

https://dspace.org/

Bromosulfophthalein inhibition of 28-kDa Schistosoma japonicum glutathione transferase: Perspectives from experimental and molecular modelling studies

Pooe, Kagiso

2022

https://hdl.handle.net/10539/34544

Downloaded from a DSpace repository. https://dspace.org/



Bromosulfophthalein inhibition of 28-kDa *Schistosoma japonicum* glutathione transferase: Perspectives from experimental and molecular modelling studies

by

Kagiso Pooe

1432394

Dissertation

Submitted in fulfilment of the requirements for the degree

Master of Science

in

Molecular and Cell Biology

in the Faculty of Science, University of the Witwatersrand, Johannesburg, South Africa

Supervisor: Dr Ikechukwu A. Achilonu

May 2022

Declaration

I, Kagiso Pooe (1432394), am a student registered for the degree of Master of Science (Dissertation) in the academic year 2022.

I hereby declare the following:

I am aware that plagiarism (the use of someone else's work without their permission and/or without acknowledging the source) is wrong.

I confirm that the work submitted for assessment for the above degree is my unaided work except where explicitly indicated otherwise.

I have not submitted this work before for any other degree or examination at this or any other University.

I have followed the required conventions in referencing the thoughts and ideas of others.

I understand that the University of the Witwatersrand may take disciplinary action against me if there is a belief that this is not my unaided work or that I have failed to acknowledge the source of the ideas or words in my writing.

signature_____ 30 th day of May 2022

Abstract

Glutathione transferases are major detoxification enzymes vital for the survival and reproduction of schistosomes during infection of the human host. The parasite expresses two GST isoenzymes, the 26-kDa and 28-kDa SjGST, showing different substrate specificities and localisations inside the parasite's tegument. Bromosulfophthalein (BSP), a diuretic compound with clinical history in liver diagnostics, has been identified and characterised as a potent Sj26GST inhibitor, showing promise as a lead molecule for the development of novel antischistosomal therapeutic drugs. This study characterises the functional, structural, and thermodynamic implications of BSP binding on Sj28GST; which has limited research attention. Enzyme kinetics show that BSP is a potent inhibitor of the enzyme, with a specific activity that decreases from 60.4 µmol min^{-1} mg^{-1} to 0.0742 µmol min^{-1} mg^{-1} and IC_{50} in the nanomolar range of 0.74 µM. Circular dichroism confirmed that purified Sj28GST follows a typical GST fold, predominantly alpha-helical. Extrinsic ANS (8-Anilino-1-naphthalene sulfonate) spectroscopy suggests that BSP binding occurs at a site distinct from the glutathione-binding site (G-site). Isothermal titration calorimetry studies show that the binding of BSP to Sj28GST is exergonic (ΔG = -34 kJ mol^{-1} and -31 kJ mol^{-1}) and enthalpically-driven, with a reaction stoichiometry of 1 BSP molecule per enzyme dimer. Molecular docking studies and molecular dynamics simulations indicate that BSP shows preferential binding to a site at the enzyme's dimeric interface, relative to the G-site and substrate binding site (H-site). The stability of Sj28GST (4.7 kcal mol^{-1}) is notably lower than Sj26GST, owing to differences in the enzyme's dimer interfaces. The findings of this study provide further insights into the binding and inhibitory behaviour of BSP on schistosome GSTs, as a potential candidate for the development of novel antischistosomal chemotherapeutics to attenuate the debilitating effects of Schistosomiasis.

Dedication

For my dear aunt, Mabatho Louise Khumalo

''Once we accept our limits, we go beyond them''

-Albert Einstein

Acknowledgements

My supervisor, Dr Ikechukwu Achilonu for his guidance and encouragement throughout my project.

Members of the Protein Structure-Function Research Unit for support and assistance.

My family and friends for their support and prayers.

The South African Department of Water and Sanitation and the Wits Postgraduate Merit Award for financial assistance.

Contents

Declaration ii
Abstract iii
Dedication iv
Acknowledgements v
List of figures ix
List of tables x
Abbreviations xi
Chapter 1 1
Introduction and research approach 1
1.1 Problem statement 1
1.2 Rationale 5
1.3 Novelty 6
1.4 Aim and objectives 7
Chapter 2 8
Literature review 8
2.1 Treatment and prevention of Schistosomiasis: Praziquantel 8
2.2 Parasite life cycle and disease pathology 10
2.3 Parasite redox biology 14
2.4 GST superfamily of detoxification enzymes 16
2.5 Schistosome GSTs 16
2.6 Sj28GST subunit structure 17
2.7 Sj28GST subunit interface 17
2.8 Stability of Schistosome GSTs 20
2.9 Catalytic function 21
2.10 Thermodynamics of ligand binding 23
2.11 BSP binding to cytosolic GSTs 24
2.12 Computational approaches to studying protein-ligand interactions 27
Chapter 3 29
Experimental procedures 29

3.1 Materials 29
3.2 Vector preparation and transformation of host cells 29
3.3 Small-scale expression of Sj28GST 31
3.4 SDS-PAGE 31
3.5 Large-scale expression of Sj28GST 32
3.6 Cell lysis and purification of Sj28GST 32
3.7 Quantification of Sj28GST 33
3.8 Far-UV circular dichroism 34
3.9 Extrinsic ANS fluorescence 36
3.10 Steady-state kinetic studies 38
3.11 Isothermal titration calorimetry 40
3.12 Urea-induced equilibrium studies 40
Chapter 4 43
Computational Procedures 43
4.1 Molecular docking of ANS and BSP on Sj28GST 43
4.2 Molecular dynamics simulations 43
Chapter 5 45
Experimental Results 45
5.1 Small-scale expression 45
5.2. Large-scale expression and purification 45
5.3. Quantification and purity assessment 45
5.4 Far-UV Circular dichroism 49
5.5 Extrinsic ANS fluorescence 50
5.6 Steady-state kinetic studies 52
5.7 Thermodynamics of Sj28GST: BSP binding: ITC 56
5.8 Conformational stability studies: urea-induced equilibrium studies 57
Chapter 6 60
Computational results 60
6.1 Molecular modelling studies 60

6.2 Molecular dynamics simulation studies 63
Chapter 7 66
Discussion 66
7.1 Overexpression, purification and quantification of Sj28GST 66
7.2 The secondary structure of Sj28GST is predominantly alpha-helical 68
7.3 ANS is displaced by BSP from Sj28GST 68
7.4 BSP inhibits the CDNB-GSH conjugation activity of Sj28GST 69
7.5 BSP binding to Sj28GST is enthalpically-driven 70
7.6 Computational analysis of Sj28GST: BSP binding 72
7.7 Sj28GST has a lower conformational stability than Sj26GST 73
7.8 Overall conclusion, limitations and future work 74
References 75

List of figures

Figure 1.1 The global distribution and prevalence of schistosomiasis 3

Figure 1.2 The distribution and prevalence of Schistosomiasis in South Africa 4

Figure 2.1 *R*- and *S*- praziquantel 9

Figure 2.2 Physiological manifestations of Schistosomiasis 12

Figure 2.3 The life cycle of the *Schistosoma* parasite 13

Figure 2.4 ROS neutralisation by schistosome antioxidant enzymes 15

Figure 2.5 Ribbon diagram showing the predicted model of Sj28GST 18

Figure 2.6 The subunit interfaces of different cytosolic GST classes 19

Figure 2.7 General catalysis reaction of glutathione transferase enzymes 21

Figure 2.8 Key residues involved in glutathione and electrophilic substrate binding in Sh28GST 22

Figure 2.9 The chemical structure of BSP 26

Figure 3.2 A schematic map of the pET-28a (+) vector. 30

Figure 3.2 A homology model of Sj28GST shown in its monomeric form 35

Figure 3.3 8-anilino-1-naphthalene sulfonate (ANS) 37

Figure 3.4 A scheme of the CDNB-GSH conjugation assay 39

Figure 5.3 SDS-PAGE analysis of Sj28GST (red box) overexpression 47

Figure 5.4 Quantification and spectral properties of purified Sj28GST 48

Figure 5.3 Far-UV CD spectrum of Sj28GST 49

Figure 5.4 Extrinsic ANS fluorescence of BSP binding to Sj28GST 51

Figure 5.5 Specific activity and IC_{50} studies of BSP on Sj28GST activity 53

Figure 5.6 Summary of the effects of BSP on the steady-state kinetic parameters of Sj28GST. 54

Figure 5.7 Isothermal titration profile of BSP binding to Sj28GST 57

Figure 5.8 Summary of conformational stability studies for Sj28GST 60

Figure 6.5 Homology modelling, validation, and sequence alignment of Sj28GST 62

Figure 6.6 Induced fit ligand docking of ANS and BSP to Sj28GST 63

Figure 6.3 Summary of the simulation trajectories over 250 ns 65

Figure 6.4 Summary of key interactions involved in ANS and BSP binding to Sj28GST 66

List of tables

Table 1: Summary of unfolding and refolding samples set-up 42
Table 2: Kinetic parameters of Sj28GST in the presence and absence of BSP..... 55

Abbreviations

AIDS	Acquired immune-deficiency syndrome
ANS	8-Anilino-1-naphthalene sulfonate
BSP	Bromosulfophthalein
CD	Circular dichroism
CDNB	1-Chloro-2,4-dinitrobenzene
DMSO	Dimethylsulfoxide
DNA	Deoxyribonucleic acid
DTT	Dithiothreitol
EDTA	Ethylenediaminetetraacetic acid
G-site	Glutathione binding site
GSH	Glutathione
GST	Glutathione transferase
GTX	S-hexylglutathione
hGSTA1	Human alpha class glutathione transferase
hGSTP1	Human pi class glutathione transferase
HIV	Human immune deficiency virus
H-site	Electrophilic substrate binding site
IC_{50}	Half-maximal inhibitory concentration
IPTG	Isopropyl β-D-1-thiogalactopyranoside
ITC	Isothermal titration calorimetry
$kcat/K_M$	Catalytic efficiency
K_d	Dissociation constant
kDa	Kilodalton
K_M	Michaelis-Menten constant
L-site	Ligand-binding site
MD	Molecular docking and molecular dynamics
MRW	Mean residue weight
MW	Molecular weight
NPT	Constant number (N), Pressure (P), and temperature (T)
NVT	Constant number (N), volume (V), and temperature (T)
OD	Optical density

PAGE	Polyacrylamide gel electrophoresis
PBS	Phosphate-buffered saline
PDB	Protein data bank
PMSF	Phenylmethylsulfonyl fluoride
PZQ	Praziquantel
RNA	Ribonucleic acid
RMSD	Root mean square deviation
RMSF	Root mean square fluctuation
ROS	Reactive oxygen species
SAPH	Schistosomiasis-associated pulmonary hypertension
SDS	Sodium dodecyl sulphate
SJ	*Schistosoma japonicum*
SOC	Super optimal broth with catabolite repression
SOD	Superoxide dismutase
TCEP	Tris(2-carboxyethyl) phosphine
TEMED	N, N, N’, N'-tetramethyl ethylenediamine
UV	Ultraviolet
V_0	Initial velocity
V_{max}	Maximum velocity
WHO	World health organisation
YT	Yeast extract and tryptone media

Chapter 1
Introduction and research approach

1.1 Problem statement

The global health impact of neglected tropical diseases remains grossly unacknowledged and under-reported. This is due to disparities in global resources and research distribution, described as the 90/10 gap. Although 90% of the world's preventable diseases occur in third-world and developing countries, only 10% of global health resources are allocated to research and drug development (Commission on Health Research for Development, 1990). Schistosomiasis, commonly known as bilharzia, is one of such neglected diseases. Schistosomiasis is caused by trematode helminths from the genus Schistosoma, which invade their human hosts through exposure to contaminated fresh water, mainly in tropic and sub-tropic regions. A previous belief was that the presence of parasitic helminths in the human body is asymptomatic and non-pathogenic, and therefore medical care was unnecessary (Warren, 1982). However, according to the World Health Organization's (WHO) conservative estimates, 220 million people required prophylactic treatment for schistosomiasis in 2017, of which less than half (102 million) were treated. In 2016, WHO's disease burden estimates also found that schistosomiasis contributed to 24 000 annual mortalities globally (World Health Organization, 2016).

The highest prevalence of schistosomiasis is in Africa, where 90% of global cases have been reported (Figure 1.1), where disease burdens are highly prevalent in impoverished communities where there is a lack of clean, potable water. Prevalence is higher amongst school-aged children, resulting in implications on growth and development (World Health Organization Geneva, 2014). In South Africa, over 4 million people, particularly school-aged and pre-school-aged children, require treatment against the parasitic disease annually (Kundai et al., 2018). This number is also likely to be grossly underestimated due to clinical misdiagnosis and a lack of updated data since prevalence is high in remote, underprivileged communities where access to primary health care is limited. Endemic areas constitute a quarter of the country, including northern parts of Limpopo and eastern parts of Mpumalanga and KwaZulu-Natal where slow-moving bodies of freshwater are found (Quayle et al., 2010) (Figure 1.2).

Strategies for controlling and eradicating schistosomiasis have focused on preventative therapy through mass drug administration. This approach has significantly reduced disease prevalence and morbidities in the Americas and Eastern Mediterranean countries. In Asia, China has shown successful control and eradication of the epidemic, however, prevalence is still high in The Philippines. Access to preventative therapy and proper water and sanitation strategies are all interventions required to diminish disease prevalence. WHO also acknowledges the limitations associated with the sole anthelminthic drug, Praziquantel (PZQ) and has outlined the need to develop new medicines as research priorities for schistosomiasis control (World Health Organization, 2015).

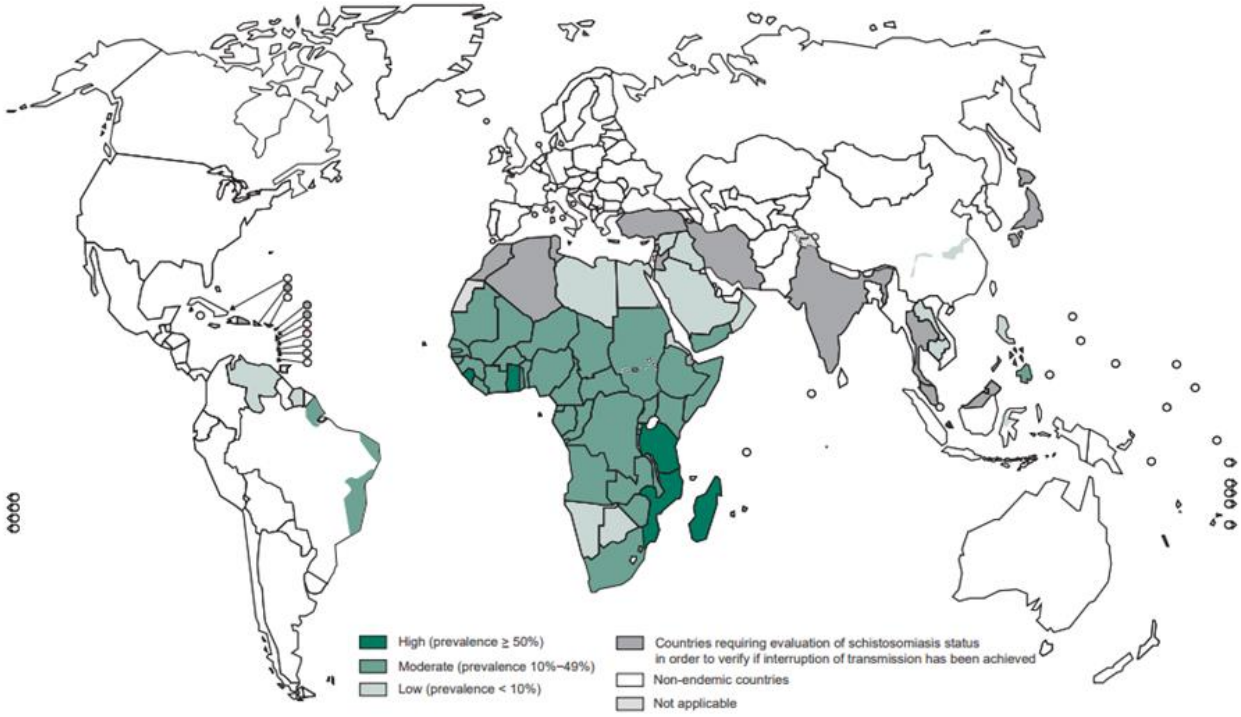


Figure 1.1 The global distribution and prevalence of schistosomiasis. Disease burdens are highly predominant in Sub-Saharan Africa where 90% of global schistosomiasis cases are reported. Adapted from The Third WHO report on neglected tropical diseases 2015.
(https://www.who.int/neglected_diseases/9789241564861/en/)

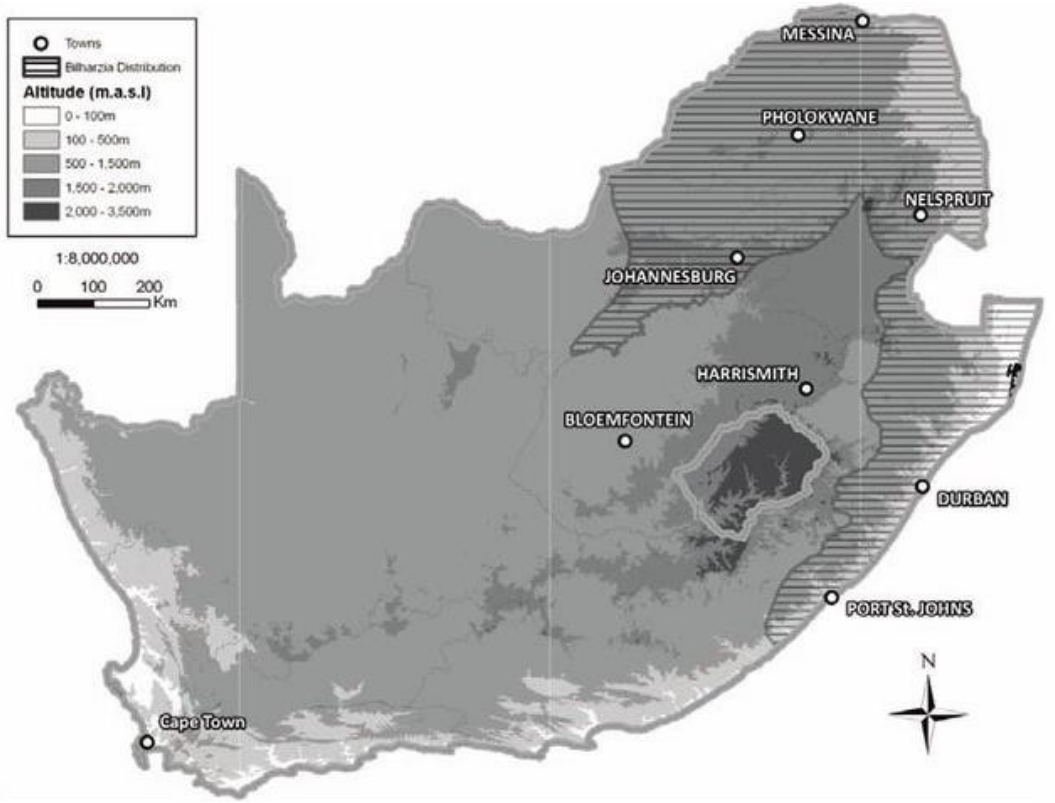


Figure 1.2 The distribution and prevalence of Schistosomiasis in South Africa. Areas of Limpopo, Mpumalanga and Kwa-Zulu Natal show the highest disease burdens in the country. Adapted from (Quayle et al., 2010)

1.2 Rationale

Glutathione transferases (GSTs) are a ubiquitous family of detoxification enzymes that catalyse the conjugation of the antioxidant, glutathione (GSH) to electrophilic and hydrophobic substrates. GSTs are also involved in the cell's uptake and transport of xenobiotic compounds. Schistosomes do not express phase one detoxification enzymes (Cytochrome p450s). They therefore solely depend on GSTs for detoxification, including the inactivation of host-mediated oxidative stress. WHO has also identified schistosome GSTs as suitable targets for vaccine and drug development. This is due to their abundant distribution across the parasite's developmental stages and their vital role in the parasites survival inside the host (Cardoso et al., 2003). Vaccine development for schistosomiasis has faced challenges due to complex interactions between host immunity and the parasite life cycle. Anti-schistosomal vaccines need to induce an immune response in the host that is stronger than the natural infection (Siddiqui et al., 2011). This emphasises the need to develop novel anti-schistosomal drugs that can serve as alternatives to the current and sole anti-schistosomal chemotherapeutic drug, praziquantel (PZQ).

Two isoforms of GST are expressed inside the parasite: the 26-kDa and 28-kDa isoforms. Each isoform has distinct distributions and substrate specificities inside the parasite. In addition to GSH conjugation to electrophilic substrates, cytosolic GSTs are also known as ligandins due to their ability to bind non-substrate ligands. However, these ligandin properties are poorly characterised (Sayed et al., 2002). Non-substrate ligand binding may inhibit catalytic activity, providing a rational approach for novel anti-schistosomal drug discovery. A crystal structure of Sj26GST in complex with PZQ has shown that the drug binds to a non-substrate binding site at the enzyme's dimer interface (McTigue et al., 1995), however, the enzyme's catalytic activity is unaffected by this binding (Milhon et al., 1997). Inhibiting catalysis with alternative ligands could provide a scaffold for novel anti-schistosomal drug discovery.

Bromosulfophthalein (BSP) is a phthalein dye commonly used in liver function tests. It is known that BSP binds to the 26-kDa isoform and inhibits its catalytic activity non-competitively (Yassin et al., 2004). Empirical studies have also shown that the drug is a potent inhibitor of the enzyme's catalytic activity (Pooe et al., 2021). These studies were supplemented with computational studies, where molecular docking and molecular dynamics (MD) studies were employed to identify the BSP binding site. These studies showed stable,

entropically-driven binding at the enzymes dimer interface, suggesting that BSP inhibition is non-competitive due to allosteric binding (Pooe et al., 2021).

To develop potent, effective anti-schistosomal drugs using GST as a molecular target, both isoforms of the enzyme need to be targeted and inhibited by the compound of interest. This study, therefore, aimed to extend BSP as an inhibitor of the 28-kDa isoform (Sj28GST). Given the structural and functional differences between the two isoforms, thermodynamics and stability studies were also employed to compare the thermodynamics of ligand binding and the conformational stability of the enzyme relative to those previously determined for Sj26GST. Lastly, MD studies were also used to support empirical observations.

1.3 Novelty

Research attention, including structural functional and ligandin properties has been directed towards the 26 kDa isoform of SjGST. Each isoform is expressed variably in the parasite's life cycle and has distinct substrate specificities. This study aimed to close the current research gap in the structural and functional characteristics of the 28 kDa SjGST isoform. An optimised expression protocol is extensively described and produces high yields of recombinantly-expressed protein. For the first time, the effects of BSP on the activity of the protein are described using enzyme activity assays. A combination of computational and thermodynamic studies is also employed to elucidate the binding site of the inhibitor on the protein dimer. Lasty, this study is the first to describe the conformational stability of the enzyme, which is influenced by the type of inter-dimeric interaction.

1.4 Aim and objectives

The project aimed to determine the inhibitory potential of BSP on Sj28GST and investigate the structural and functional basis of the enzyme-inhibitor interaction. This aim was achieved with the following objectives:

1. Heterologous expression of Sj28GST with the pET-28a (+) vector in *E. coli* cells and purification with GSH-agarose affinity chromatography.
2. Structural analysis of Sj28GST with far-UV circular dichroism spectroscopy (Far-UV CD) and extrinsic fluorescent spectroscopy using 8-anilino-1-naphthalenesulfonate (ANS).
3. Investigating the effects of BSP on the specific activity of Sj28GST using the glutathione-1-chloro-2,4-dinitrobenzene (GSH-CDNB) conjugation activity assay with absorption spectroscopy.
4. Determination of the half-maximal inhibitory concentration (IC_{50}) of BSP on Sj28GST activity using the GSH-CDNB conjugation assay
5. Determination of the Michaelis-Menten kinetic parameters, V_{max}, K_M and k_{cat}/K_M of Sj28GST in the presence and absence of BSP.
6. Isothermal titration calorimetry (ITC) for the determination of the reaction stoichiometry, K_d, as well as the thermodynamic parameters (ΔG, ΔH, ΔS) of BSP binding to Sj28GST.
7. Conformational stability studies using urea-induced equilibrium studies.
8. Molecular Modelling and Molecular Dynamics (MD) studies to computationally define the binding behavior of BSP to Sj28GST.

Chapter 2
Literature review

2.1 Treatment and prevention of Schistosomiasis: Praziquantel

To date, mass drug administration prevention strategies have depended on the administration of Praziquantel/PZQ (2-cyclohexylcarbonyl-l,3,4,6,7,11b-hexahydro-2H-pyrazino [2,1-a] isoquinolin-4-one). The drug was first identified in the 1970s from a library of pyrazinoquinolinone derivatives for its anthelmintic activity against a broad range of cestode and trematode worms (Seubert et al., 1977). For decades, PZQ treatment has shown adequate schistosomiasis control in endemic regions due to its affordability (0,2-0,3 USD), low therapeutic dosage (40-60 mg/kg) and acute side effects (Gabrielli et al., 2006; World Health Organization, 2006). Also, the drug is freely available in highly endemic countries in Sub-Saharan Africa.

PZQ has, however, a few shortcomings which have prevented the complete eradication of Schistosomiasis in endemic countries. Firstly, PZQ is administered as a racemic mixture of R- and S- enantiomers (Figure 2.1). Only the R- enantiomer exhibits anti-schistosomal activity, and the latter is responsible for the drug's bitter taste, which poses challenges for oral administration to school-aged children (Meyer et al., 2009). The sole dependence on PZQ for schistosomiasis control has also led to increasing concerns about developing resistant strains. Although PZQ resistant worms have not yet been identified in African schistosomes, the increasing widespread endorsement of PZQ as the anti-schistosomal drug of choice is likely to enforce selective pressure for the evolution of PZQ resistant strains. In Egypt, evidence for possible resistance was shown with patients who had frequent re-infections after three PZQ treatments having schistosome isolates that were less sensitive to the drug than isolates from successfully treated patients (Ismail et al., 1999).

The exact molecular mode of action of PZQ remains unclear. PZQ exposure has been linked to the rapid uptake of Ca^{2+} ions in adult schistosomes resulting in muscular contractile paralysis and tegument vacuolisation (Cioli and Pica-Mattoccia, 2003; Park and Marchant, 2020). This lack of fundamental knowledge regarding the drug's mode of action provides a bottleneck in research and development for novel anti-schistosomal drugs. Lastly, the drug has proven to

only be effective against the egg and adult male developmental stages, resulting in frequent re-infections and incomplete eradication of worm burdens in patients.

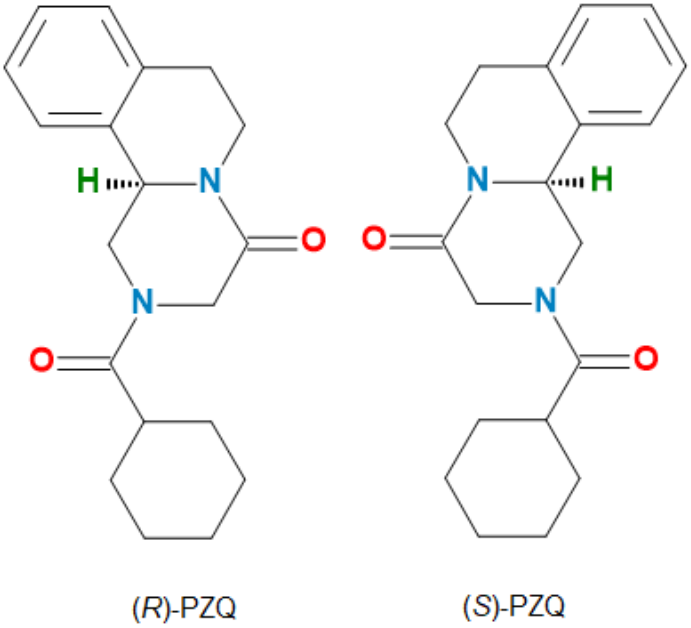


Figure 2.1 *R*- and *S*- praziquantel.Generated with BIOVIA Draw 2019. (https://hts.c2b2.columbia.edu/draw/)

2.2 Parasite life cycle and disease pathology

There are six main schistosomiasis-causing species: *S. mansoni*, *S. japonicum*, *S. haematobium*, *S. mekongi*, *S. intercalatum* and *S. guinesis*. Each species has distinct geographical locations specific to the habitats of its intermediate snail hosts. The three most prevalent of these are *S. mansoni* (Africa, the Americas and the Middle East), *S. japonicum* (China and the Philippines) and *S. haematobium* (Africa and the Middle East). *S. japonicum* is responsible for chronic intestinal schistosomiasis and is transmitted by intermediate snail hosts belonging to the genus *Oncomelania* (Roberts et al., 1996).

The life cycle (Figure 2.3) of the parasite involves penetration of the skin by free-swimming schistosomal cercariae, which travel through the lungs into the mesenteric venous system where maturation and mating of the female and male worms occur (Roberts et al., 1996). After mating, the female worm travels to the mesenteric venules and lay between 300 to 3000 eggs per day, which invade the gut mucosa and ultimately expelled the faeces. Once inside freshwater, eggs hatch into miracidia. They infect intermediate snail hosts, which multiply to release at least thousands of cercariae that will penetrate the human host upon exposure to contaminated fresh water (Warren, 1982).

The pathogenicity of schistosomal infections is mainly attributed to the egg stages of the life cycle as opposed to the mature developmental stages. Chronic infections are caused by the secretion of proteolytic enzymes from schistosome eggs lodged in the host's tissues. These enzymes in turn incite granulocyte or eosinophil-induced inflammation and fibrosis (Colley et al., 2014). Within a day of exposure to the parasites' cercariae, acute dermatitis may result in the skin; characterised by itchy lesions. *S. japonicum* is also the main causative agent of Katayama fever (acute schistosomiasis) which lasts for several weeks, including fever, coughing, fatigue, and abdominal discomfort. Intestinal schistosomiasis causes persistent, debilitating abdominal pain, severe diarrhoea, and appetite loss (Gryseels et al., 2006).

Female genital schistosomiasis has been associated with increased susceptibility to HIV infections. *S. haematobium*, the main causative species of genital schistosomiasis localizes its eggs in the female reproductive organ. This presents many pathophysiological symptoms which promote viral entry during sexual intercourse. These symptoms include a variety of lesions on the vulva, vagina and cervix, which are easily bruised upon contact (Feldmeier et al., 1994). The unacknowledged prevalence of schistosomiasis in endemic countries, mainly in Africa, has contributed to the unabated spread of HIV/AIDS.

Chronic schistosomiasis also affects early childhood development. Frequent re-infections in school-aged children and pre-adolescents contributes to fibrosis of vital organs in adulthood and contributes to anaemia, growth stunting, and cognitive impairment (Gurarie et al., 2011) (Figure 2.3). Schistosomiasis-associated pulmonary hypertension (SAPH) is the most prevalent manifestation of chronic schistosomiasis. Migration of *S. mansoni* eggs to the hepatoportal veins incites pre-portal fibrosis and inflammation, a pre-condition of pulmonary hypertension. SAPH is also the most common form of pulmonary hypertension, with an estimation of over 270 000 people affected worldwide (Graham et al., 2010; Lapa et al., 2009).

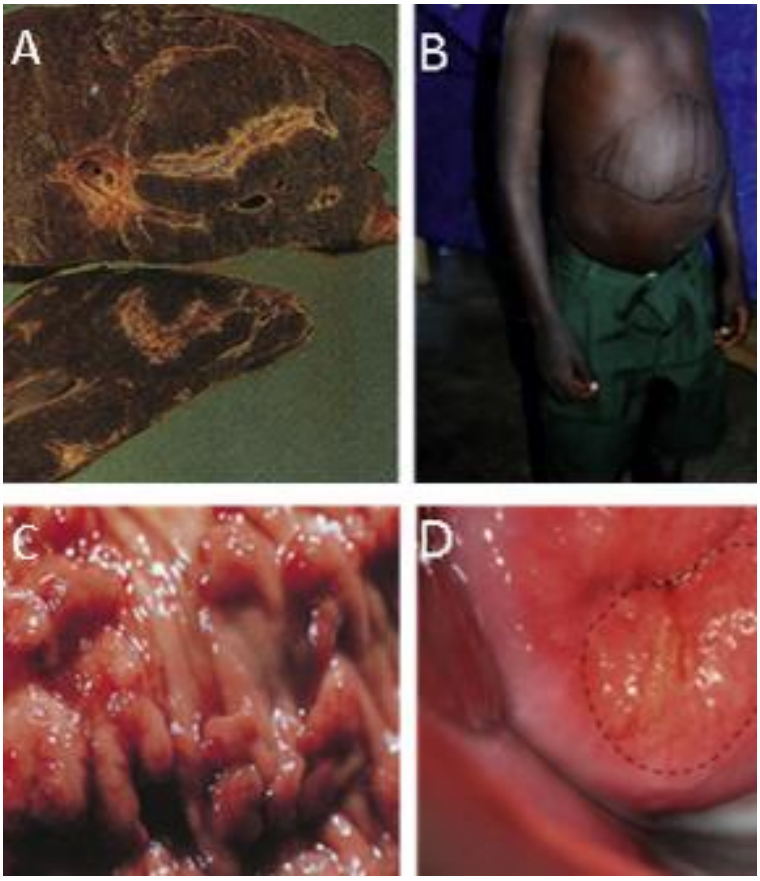


Figure 2.2 Physiological manifestations of Schistosomiasis. Common manifestations include hepatic fibrosis (A), expanded abdominal veins (B), Gastrointestinal disease (C) and cervical lesions (D). Adapted from (Nabarro et al., 2018)

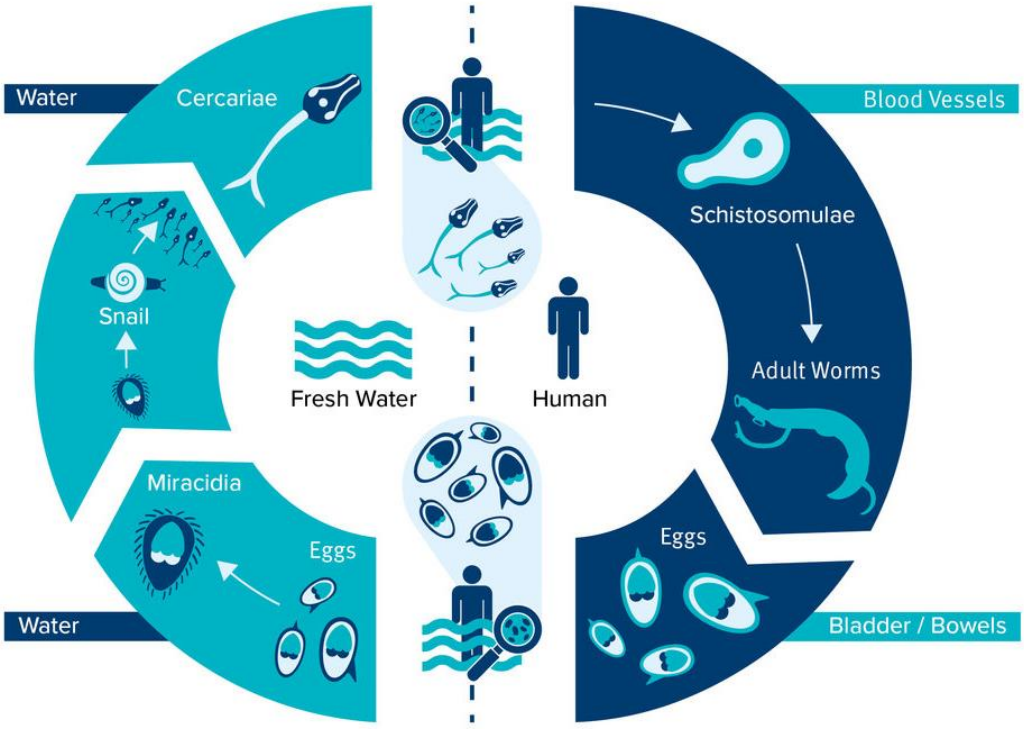


Figure 2.3 The life cycle of the *Schistosoma* parasite. Schistosomal cercariae infiltrate the skin and swim through the lungs into the hepatoportal system where maturation and mating of the adult developmental stages occur upon exposure to contaminated fresh water. Following mating, adult females migrate to the gastrointestinal system (*S. mansoni* and *S. japonicum*) or the urogenital system (*S. haematobium*) where thousands of eggs are laid and passed through the faeces or urine into freshwater. This is followed by hatching and the emergence of the miracidia. This free-swimming stage infects the intermediate snail host and produces consecutive generations of sporocyst. Cercariae are released after several weeks. Adapted from the schistosomiasis control initiative foundation website. (https://schistosomiasiscontrolinitiative.org/sch)

2.3 Parasite redox biology

Oxidative stress defence through reactive oxygen species (ROS) is the foremost hurdle encountered by schistosomes upon host infection (Huang et al., 2012). The generation of free radicals such as ROS and reactive nitrogen species (RNS) is due to normal cellular metabolic processes such as the premature "leaking" of electrons to oxygen in the mitochondrial electron transport chain during aerobic respiration, generating the highly reactive superoxide anion(O2•-) (Cadenas and Davies, 2000). In low concentrations, free radicals provide advantageous effects, including activating mitogenic signals. Due to their highly reactive nature, the generation of free radicals and their neutralization is tightly regulated by families of antioxidant enzymes to maintain the redox balance of cells (Valko et al., 2007).

Free radical build-up causes adverse effects on cells, such as damage to cellular components including DNA, proteins and lipid membranes (Valko et al., 2007). Host immune cells produce ROS as a humoral cytotoxic response to induce oxidative stress in parasite cells. As a defence mechanism, schistosomes have evolved several antioxidant enzymes, showing restricted of antioxidant enzymes across the developmental stages, with early stages having increased susceptibility compared to the adult stages, which express higher levels of antioxidant mRNA (LoVerde, 1998). Expression of the antioxidant enzymes, glutathione transferase (GST), signal peptide-containing superoxide dismutase (SP-SOD), glutathione peroxidase (GPx) and cytosolic superoxide dismutase (CT-SOD) has been shown to play a vital role in the evasion of host immunity, with GST showing the highest expression levels in the egg and mature female stages whilst the other proteins expressed an abundant localization in the gut epithelia and teguments of adult schistosomulae (Mei and LoVerde, 1997).

Antioxidant enzymes in parasitic cells evade host-induced oxidative damage through the neutralization of ROS in a stepwise manner (Figure 2.4). Targeting these enzymes through drug inhibition is therefore a rational approach to combat schistosome survival inside the human host. SOD converts the superoxide anion ($O_2^{\bullet-}$) into hydrogen peroxide (H_2O_2), which is then decomposed by the catalase enzyme (McCord and Fridovich, 1969). The lack of catalase in parasitic helminths is due to their facultative anaerobic metabolism. Because they rely on anaerobic respiration for energy production, ROS are rarely produced through the electron transport chain, and low levels of H_2O_2 do not render significant cellular damage (McCord et al., 1971). The production of ROS through metabolism is also reduced in schistosomes by switching from aerobic to anaerobic metabolism during the blood-residing developmental stages (Oliveira and Oliveira, 2002). H_2O_2 can also be neutralised by GPx through GSH

oxidation, producing water and glutathione disulfide (GSSG), which subsequently undergoes reduction by glutathione reductase (Chiumiento and Bruschi, 2009). GPx also neutralises lipid hydroperoxides, and its localization to the adult gut epithelium and the tegument suggests that the enzyme plays a role in protecting lipid membranes against ROS damage (Huang et al., 2012). Overall, antioxidant enzymes can be regarded as major pathogenic factors through the catalysis of redox reactions involved in neutralising oxidative damage. One of the most pivotal enzymes is the glutathione transferase family, which is ubiquitous and catalyses the conjugation of the antioxidant, GSH to various substrates.

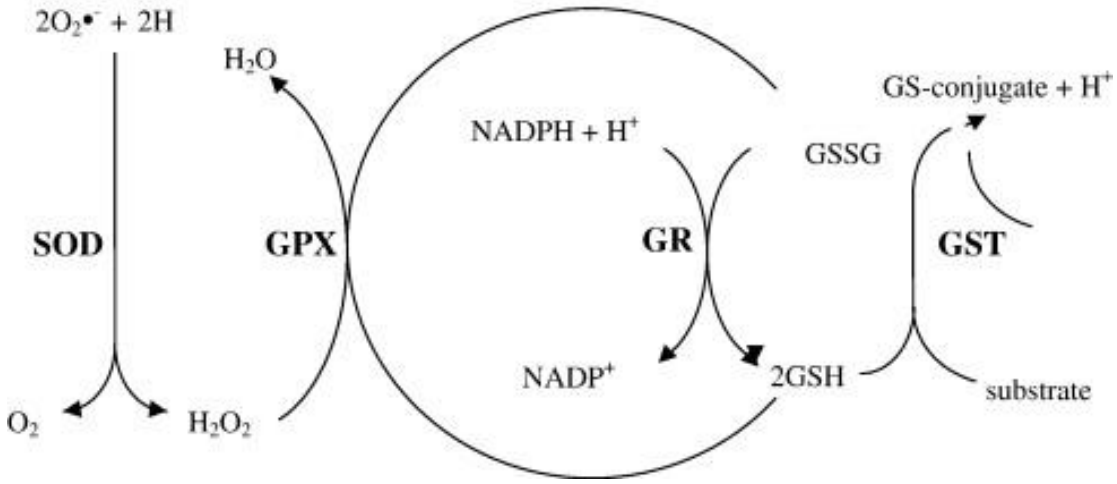


Figure 2.4 ROS neutralisation by schistosome antioxidant enzymes. Superoxide anion is formed through the reduction of molecular oxygen with reducing equivalents in the form of NADPH. Dismutation of the superoxide anion is catalysed by superoxide dismutase (SOD) into hydrogen peroxide (H_2O_2). GSH provides an electron for the decomposition of H_2O_2 by glutathione peroxidase (GPx). Oxidised glutathione/glutathione disulfide (GSSG) is reduced by NADPH, regenerating GSH through the catalysis of glutathione reductase (GR). Glutathione transferase (GST) conjugates GSH to electrophilic substrates. Adapted from (Yan et al., 2008)

2.4 GST superfamily of detoxification enzymes

The tripeptide, GSH (γ-l-glutamyl-l-cysteinyl-glycine) acts as a major antioxidant in cells, maintaining the redox balance of the cell through the sustenance of high ratios of GSH/GSSG (Figure 2.4) to counteract oxidative stress mechanisms (Valko et al., 2007). GSH can directly scavenge and neutralise free radicals in the cell or serve as a cofactor for GPx or GST detoxifying enzymes. The GST enzyme family members (EC 2.5.1.18) are responsible for increasing the activity and inactivating the toxic effects of exogenous and endogenous compounds. This is through the increased solubility of substrates, serving as the initial steps of the mercapturic pathway (Cardoso et al., 2003). Substrates include xenobiotics such as chemotherapeutics, environmental pollutants, steroids, hormones and carcinogens (Listowsky et al., 1988). Cytosolic GSTs can be homodimeric or heterodimeric, with a glutathione-binding site (G-site) at the N-terminus and a more variable, alpha-helical substrate-binding site (H-site) at the C-terminal domain (Cardoso et al., 2003). They are classified into eight groups (alpha, pi, mu, theta, sigma, omega, kappa and zeta) based on their amino acid composition (Cvilink et al., 2009). The amino acid sequence similarity is the highest within the GST classes (80%) compared to between classes (40%) (Wilce and Parker, 1994).

2.5 Schistosome GSTs

The absence or low occurrence of phase I detoxification enzymes in parasitic helminths renders the GSTs the major antioxidant enzymes. Phase I detoxification is catalysed by cytochrome P450 enzymes. It involves the conjugation of radicals such as the hydroxyl radical to xenobiotic substrates using molecular oxygen and NADPH, producing reactive conjugates for further metabolism by the phase II detoxification enzymes (Liska, 1998). GSTs are highly represented across all parasitic helminths and have two principal functions, i) Glutathione conjugation to haematin, thus resulting in solubilisation to prevent blockage of the parasite's gut and ii) The inactivation of secondary products of lipid peroxidation to circumvent host-induced oxidative damage (Cardoso et al., 2003). Two isoforms of GST have been detected in schistosomes and are classified according to their subunit sizes, the 26-kDa and 28-kDa isoforms. The isoforms have varying kinetic properties with distinct substrate-binding functions following a sequential bi-substrate catalytic mechanism. The 26-kDa isoform is associated with GSH conjugation to reactive carbonyls, and lipid peroxides, whilst the 28-kDa GST is involved in the inactivation of exogenous xenobiotics, with restricted activity towards lipid peroxides (Walker et al., 1993).

The two isoforms also have different localisations in the parasite's tegument and sub-tegumentary cells, emphasising the distinct roles each isoform play in the redox metabolism and antioxidant defence of the parasite during infection (Porchet et al., 1994; Trottein et al., 1990).

2.6 Sj28GST subunit structure

Like other cytosolic GSTs, schistosome GSTs are constitutive dimers, with each monomer consisting of an independent, active site. Sj28GST subunits are 206 residues and follow the canonical GST fold with two domains (Figure 2.5). The N-terminal domain folds into a thioredoxin-like topology (βαβαββα) with four β-strands sandwiched between three alpha-helices and consists of the G-site. The C-terminal domain houses the H-site and folds into a bundle of 6 alpha-helices. Although the two subunits are highly similar, they are not identical (Johnson et al., 2003). Presently, there are no crystal structures of Sj28GST available on the protein data bank (PDB). However, Sj28GST shows the highest sequence homology (77%) to the 28-kDa GST from Schistosoma haematobium (Sh28GST) (PDB ID: 1OE8). A homology model was predicted using SWISS-MODEL (Waterhouse et al., 2018) and validated using PDBsum (Laskowski et al., 1997). The predicted model structure follows the canonical GST fold.

2.7 Sj28GST subunit interface

Cytosolic GSTs are classified into two groups based on their type of subunit interface (Figure 2.6). The first is the alpha/mu/pi/Sj26GST type, with a hydrophobic ball and socket type interface and few polar residues, the second is the sigma/theta type interface, which is predominantly hydrophilic and is characterised by a network of polar residues (Armstrong, 1997, Yassin et al., 2004). In the first type, a highly conserved phenylalanine residue, Phe 52, is inserted inside a hydrophobic pocket of the next subunit between alpha-helices 4 and 5. This residue is located on a loop not present in the sigma/theta type interface. In addition, two salt bridges (Asp77-Arg89 and Glu51-Arg136) are involved in inter-subunit contacts in Sj26GST. Dimer formation also results in long (40 Å) and narrow (~ 10Å) cavity which allows for the binding of non-substrate ligands (McTigue et al., 1995).

The 28-kDa schistosome GSTs are structurally homologous to the sigma class of mammalian GSTs. Therefore, they lack the C-terminal loop involved in hydrophobic contacts with the N-terminal domain of the next subunit. In addition, they also have a sigma/theta type interface

lined by hydrophilic, polar residues. The dimeric structure is predominantly stabilized by non-polar interactions with four salt bridges (Johnson et al., 2003).

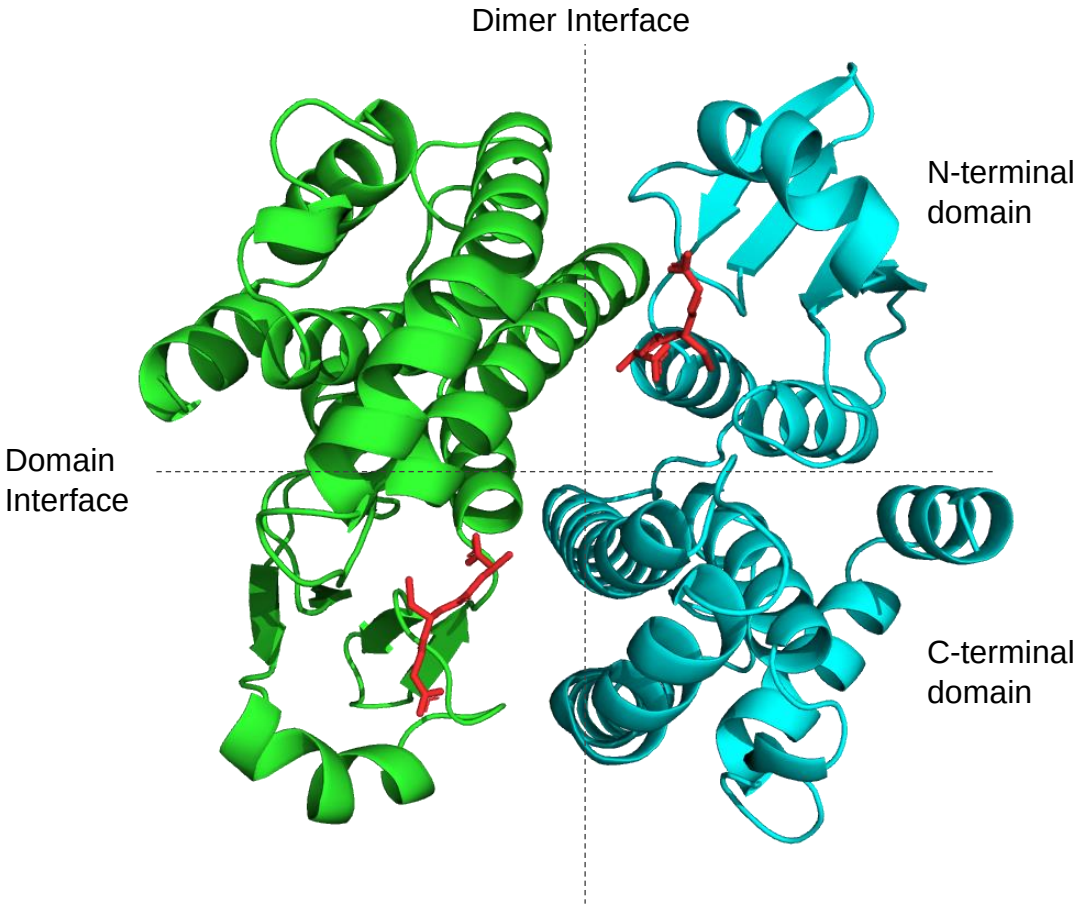


Figure 2.5 Ribbon diagram showing the predicted model of Sj28GST. Sj28GST shows the highest sequence homology (77%) to Sh28GST.The enzyme follows the canonical GST fold, with thioredoxin-like topology in the N-terminal domain and an alpha-helical C-terminal domain. The structure is represented in complex with glutathione (red). The homology model was generated using SWISS-MODEL (Waterhouse et al., 2018) using Sh28GST as a template PDB ID (1OE7). The ribbon diagram was generated using the PyMol molecular graphics program.

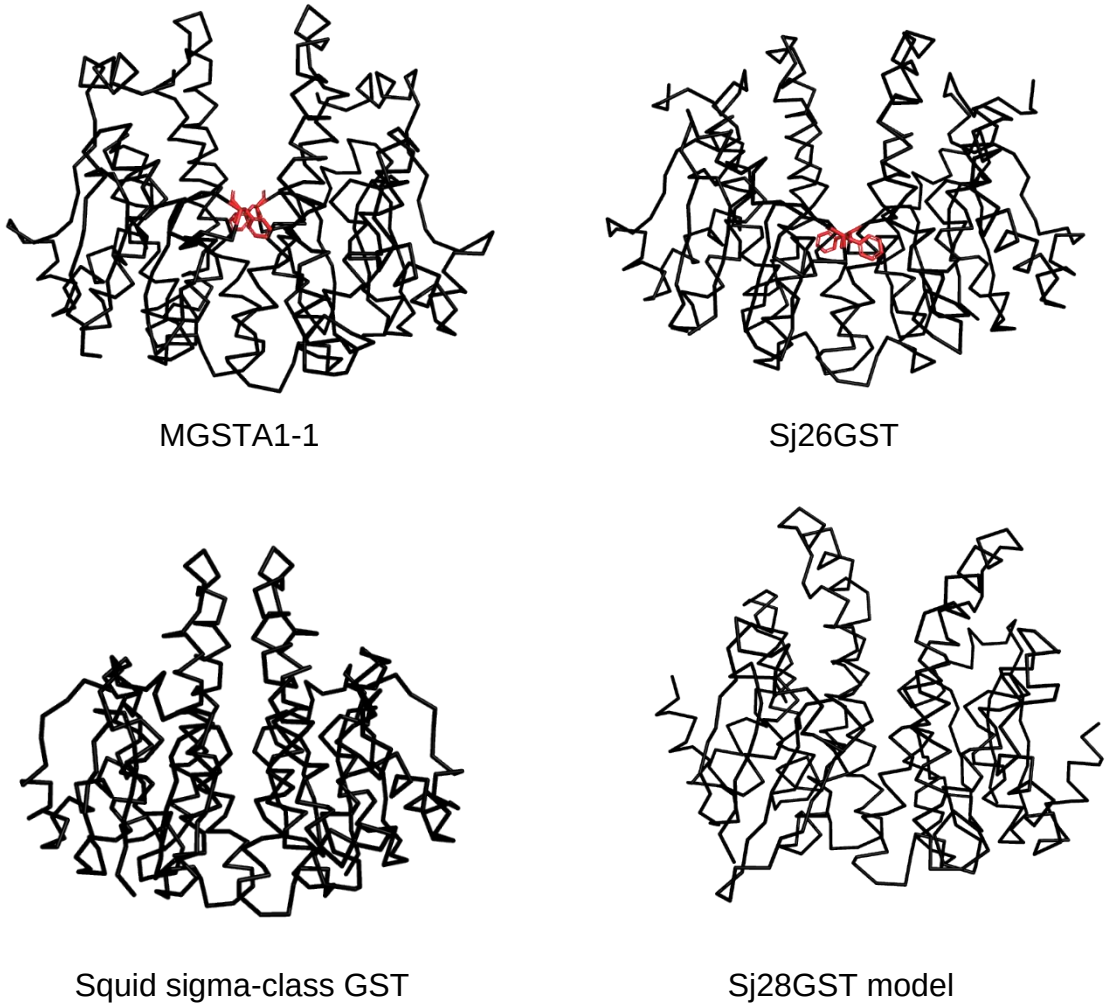


Figure 2.6 The subunit interfaces of different cytosolic GST classes. Alpha/mu/pi/Sj26GSTs are stabilised by a highly conserved phenylalanine residue (red) at the hydrophobic subunit interface. Sigma/theta/Sj28GSTs lack this lock-and-key interaction and are stabilized by a network of electrostatic interactions. The structures were generated using the PyMol molecular graphics programme.

2.8 Stability of Schistosome GSTs

The ability of newly synthesised polypeptide chains to spontaneously fold into compact, functional protein molecules has provided a functional evolutionary advantage for living organisms (Dobson, 2003). The degree of the spontaneity of a protein-folding event is directly related to the stability of the folded state. In addition, protein folding has direct functional implications. Suppose a polypeptide chain follows an improper folding path due to mutations or transcriptional/translation errors. In that case, the activity of the protein may be compromised, i.e., at key binding or active sites (Thomas et al., 1995). Therefore, studying protein folding and conformational stability has significance in understanding the relationship between protein structure and biological function (Vendruscolo et al., 2003).

The reversibility of protein folding is a key factor in protein stability. The thermodynamic hypothesis to protein folding hypothesizes that a protein molecule's native, folded conformation has the lowest possible Gibbs free energy under native conditions and is, therefore, more thermodynamically favoured over the linear, denatured state (Dobson et al., 1998). Protein folding cooperatively takes place and the linear polypeptide undergoes a folding transition/s until the state of lowest Gibbs free energy and highest thermodynamic favorability is reached (Anfinsen, 1973). Under native conditions, the conformational stability of protein molecules has been small. Factors that drive protein folding (electrostatic interactions, hydrogen bonds, disulfide bonds, hydrophobic bonds) can easily be disrupted by changing the solvent environment (Rose et al., 2006). Unfolding is typically induced by introducing chemical denaturants such as urea or increasing the temperature. The unfolding path can then be followed with various probes, including fluorescence spectroscopy or circular dichroism, providing a sigmoidal curve at which the midpoint is the folding/unfolding transition (Rose et al., 2006).

A conserved phenylalanine residue (Phe 51) in the alpha/mu/pi/Sj26 GSTs is responsible for the conformational stability of the dimeric structure (Codreanu et al., 2005). Conformational stability studies have shown that GSTs with this type of lock and key interface fold via a two-state pathway where the folded and unfolded monomers are highly populated at equilibrium. This type of folding pathway consists of no folding intermediates, suggesting that the dimeric structure stabilizes the two monomers (Erhardt and Dirr, 1995; Kaplan et al., 1997). Sigma and theta class GSTs have shown lower stability compared GSTs with the lock and key type interface due to the absence of this conserved inter-subunit interaction. Also, the folding pathway follows a multi-step path with monomeric/dimeric intermediates (Stevens et al.,

1998). Therefore, the subunit interface is of significance for both molecular recognition and the stability of cytosolic GSTs.

2.9 Catalytic function

The catalytic mechanism of GST depends on the stable dimerization of the two monomers. All GSTs carry out the glutathione conjugation reaction through the nucleophilic addition of an activated GSH thiolate by the following general equation:

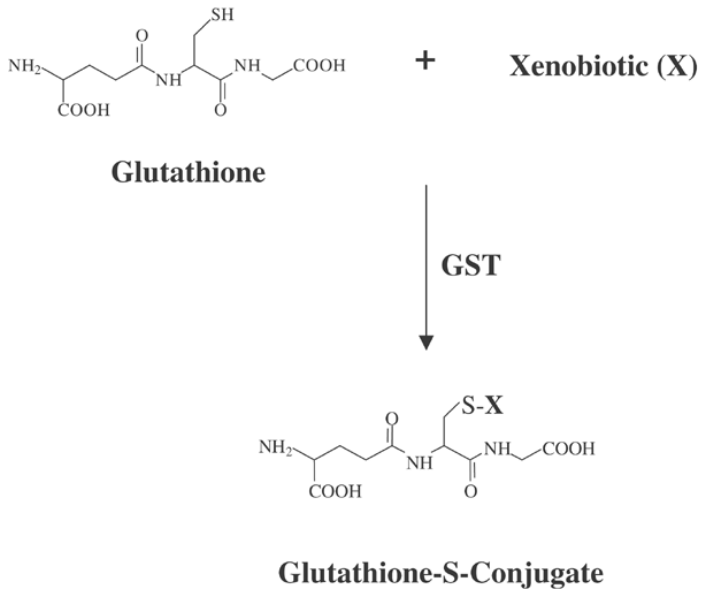


Figure 2.7 General catalysis reaction of glutathione transferase enzymes. Adapted from (Townsend and Tew, 2003)

The catalytic mechanism can be described as a sequential bi-substrate mechanism where GSH binding is likely to occur first due to its excess physiological concentration (1 mM-10 mM) (Dirr et al., 1994).

A crystal structure of the 28-kDa GST from *Schistosoma haematobium* (Sh28GST) has revealed insights into the catalysis of sigma-class GSTs (Johnson et al., 2003). In summary, G-site residues in the N-terminus are pivotal for the binding, alignment and activation of GSH through, a) The stable orientation of ɣ-glutamine, b) Carboxy-terminal stabilization of glycine and c) interactions between the thiol group on the GSH cysteine and the highly conserved Tyr 10 phenolic group for GSH activation and alignment (Lim et al., 1994).

A unique feature of Sh28GST is that the tyrosine residue occupies two distinct positions (Figure 2.8A). The first is an exterior position where the tyrosine phenol group is involved in

a π cation interaction with a neighbouring arginine residue. This interaction lowers the pKa of the tyrosine, which is a precursor for GSH activation. The second interior position is canonical for cytosolic GSTs, where the tyrosine residue faces towards the GSH thiol group and lowers the pKa of the thiol to form a thiolate ion. Interactions with 11 neighbouring residues stabilise the exterior position, whilst interactions with ten residues stabilise the interior position. Switching of the tyrosine residue between the two positions is necessary for catalysis, therefore this unique feature may present a strategy for novel antischistosomal drug design (Angelucci et al., 2005).

In the electrophilic substrate binding site, the H-site is formed in well-defined hydrophobic pockets in domain II. The 28-kDa schistosome GSTs have been found to have prostaglandin synthase activity, which regulates inhibition of the host's immune system. A crystal structure of Sh28GST in complex with the product analogue, *S*-hexylglutathione (GTX) (Figure 2.8B), shows that the site is very spacious and would allow for the placement of the prostanoid precursor near the G-site (Johnson et al., 2003).

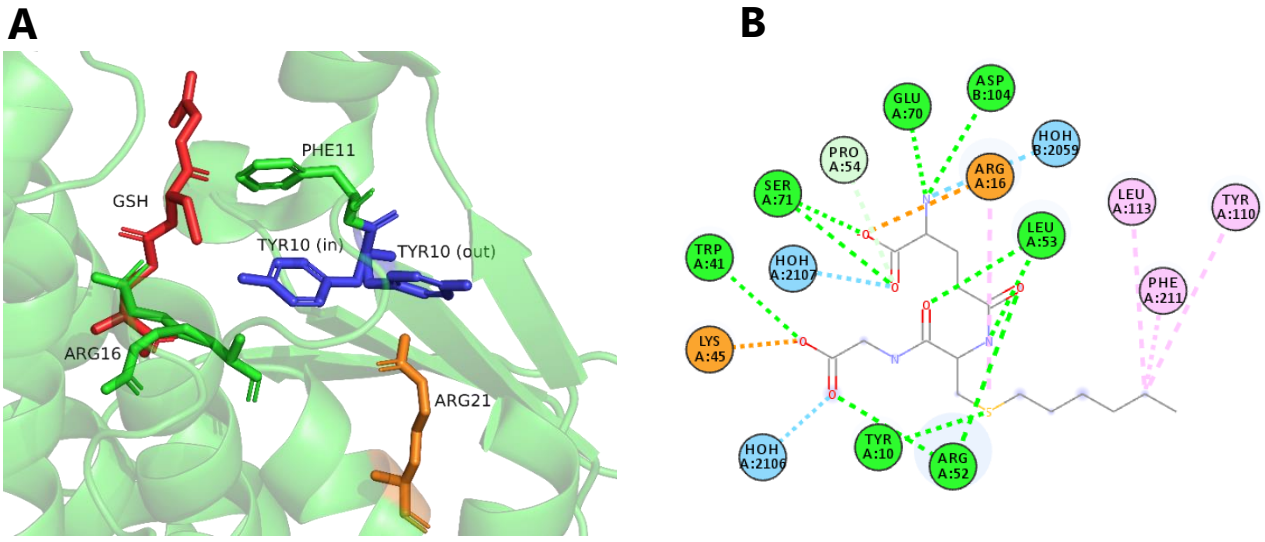


Figure 2.8 Key residues involved in glutathione and electrophilic substrate binding in Sh28GST. **A**. A catalytic tyrosine occupies two alternative positions (in and out). The out position forms a π cation interaction at hydrogen bond distance with arginine 21, decreasing the pKa of the thiol group for catalysis. The in position forms a hydrogen bond with the GSH thiol, forming a thiolate ion. Generated using the Pymol molecular graphics programme **B**. 2D ligand interaction plot of Sh28GST in complex with the product analogue; s-hexylglutathione. Ligand binding is predominantly stabilised by hydrogen bonds and 2 salt bridges.Generated using Discovery studio visualiser.

2.10 Thermodynamics of ligand binding

Isothermal titration calorimetry (ITC) allows for determining the thermodynamics of protein-ligand interactions by measuring heat changes resulting from these interactions. An ITC experiment involves the stepwise injection of the ligand/reactant solution into a reaction cell with the enzyme, producing a heat signal (qi), this signal is directly proportional to the ratio of ligand that binds during a specific injection ($v \times \Delta L_i$) and the reaction binding enthalpy (ΔH), given by the following equation.

$$qi = v \times \Delta Ln \times \Delta H \quad (\textit{Equation 1})$$

Where *v* represents the volume in the reaction cell and *Ln* is the proportion of the ligand after the nth injection. The ITC instrument measures how much power (µcal/second) is needed to keep the temperature difference between the reference and sample cell constant after each injection. (Leavitt and Freire, 2001). This is referred to as a differential power compensation design. The heat of the reaction is derived from the area under each peak or injection. This allows for the direct quantification of ΔH, reaction stoichiometry (N), and the reaction binding affinity /association equilibrium constant (K_a). Further thermodynamic parameters such as the Gibbs free energy (ΔG) and reaction entropy (ΔS) can then be derived from the following thermodynamic equations:

$$\Delta G = -RT \ln \frac{1}{Kd} \quad (\textit{Equation 2})$$

And,

$$\Delta G = \Delta H - T\Delta S \quad (\textit{Equation 3})$$

Gibbs free energy (ΔG) of ligand binding

As in any spontaneous reaction, protein-ligand interactions are thermodynamically characterised by a net negative Gibbs free energy (ΔG). ΔG can be defined from the sum of the system's enthalpic and entropic contributions (Equation 3) or related to the affinity of the protein-ligand interaction by way of the equilibrium constant as defined by equation 2 (Bronowska, 2011).ΔG defines the extent of the spontaneity of a reaction that has reached equilibrium at constant temperature and pressure and therefore serves as a useful parameter to describe the stability of the interaction. The larger the equilibrium constant, the more negative the ΔG, indicative of a higher affinity between the protein and the ligand and overall higher

stability of the resulting complex. Under standard temperature, pressure and concentration conditions, the standard Gibbs free energy of the binding is denoted as ΔG°(Du et al., 2016).

Enthalpy (ΔH) of ligand binding

The enthalpic term (ΔH) is described as the system's total energy/heat component. As defined by Hess's Law, the net change in enthalpy is obtained from the sum of the enthalpies in the reaction. In a protein-ligand interaction, contributions to the enthalpic term result from the formation or disruption of non-covalent interactions during the binding event. The net ΔH of ligand binding, therefore, encompasses the forces (hydrogen bonds, van der Waals forces, electrostatic interactions etc.) involved in the protein-ligand complex as well as the strength of these interactions. These forces include not only protein-ligand interactions but also protein-solvent as well as ligand-solvent interactions (Du et al., 2016).

Entropy (ΔS) of ligand binding

The entropy of ligand binding describes the dynamics between the protein and its binding partner. The second law of thermodynamics states that a system always approaches a state of disorder or positive entropy. The introduction or elimination of the degrees of freedom available upon a ligand binding event determines the system's degree of disorder or motion. The overall binding entropy (ΔS) can be divided into the solvation entropy (the exclusion of water molecules from buried hydrophobic regions), the conformational entropy (the conformational dynamics of the protein-ligand complex), as well as the translational/rotational entropy (describes the translational/rotational degrees of freedom upon binding) (Bronowska, 2011).

2.11 BSP binding to cytosolic GSTs

Bromosulfophthalein (Figure 2.9) is a purple phthalein dye previously utilised in clinical diagnostics of liver functioning. Prolonged retention of the drug in the bloodstream indicates liver dysfunction. Uptake and transport of BSP from the blood into the liver for excretion is mediated by GSH conjugation (Schwenk et al., 1976). As a result, the drug is a model substrate or inhibitor for cytosolic GSTs due to its ability to bind to overlapping classes, which often results in the inhibition of catalysis. Suppose schistosomal GSTs are the molecular target of choice for novel drug development. In that case, the host GST activity needs to remain uncompromised by the drug, as it serves an important role in the host's redox balance and metabolism.

A critical difference between human and schistosome GSTs appears to be the site at which BSP binds, which governs the catalytic consequences of binding. Thermodynamic studies have identified two sets of BSP binding sites per human GSTA1-1 subunit. The high and low-affinity binding sites show reaction stoichiometries of 1 and 3 BSP molecules per binding site, respectively. Although BSP is a potent hGSTA1-1 inhibitor (IC_{50} = 7 μM), binding of the drug to the high-affinity site next to the H-site (K_d =0.12 μM) does not inhibit catalysis (Kolobe et al., 2004). X-ray crystallography studies on the human GST P1 class (hGSTP1-1) have shown that large non-substrate ligands, including BSP, are accommodated by the H-site of the enzyme, which may not completely inhibit the enzyme's activity as it does not interfere with the formation of the CDNB transition-state complex (Oakley et al., 1999).

Helminth GSTs have varying substrate specificities relative to the human cytosolic GSTs. As reported by X-ray crystallographic studies, the long and narrow pocket at the subunit interface is the preferred ligand-binding site for the leading anthelminthic, PZQ, as well as a natural antioxidant, ellagic acid, to Sj26GST (Akumadu et al., 2020; McTigue et al., 1995b). Although PZQ does not inhibit the CDNB-GSH conjugation activity of the enzyme (Milhon et al., 1997), ellagic acid-binding does result in mixed inhibition of catalytic activity. This unique binding mode was also shown in a crystal structure of the sigma-class squid digestive gland GST bound to the product analogue, S-(3-iodobenzyl) glutathione (Ji et al., 1996). Cytosolic GSTs, therefore, appear to have evolved the dimer interface for ligandin binding at the cost of catalytic activity. The dimer interface has also been postulated as the ligandin site for BSP in Sj26GST. Molecular dynamics have supplemented empirical methods and molecular modelling simulations, showing that BSP binding to Sj26GST is enthalpically-driven and entropically favoured, resulting in non-competitive inhibition of activity due to allosteric binding to the dimer interface (Pooe et al., 2021; Yassin et al., 2004). This study aims to provide context into the ligand-binding properties of BSP to Sj28GST, which has not been extensively studied relative to the 26-kDa isoform.

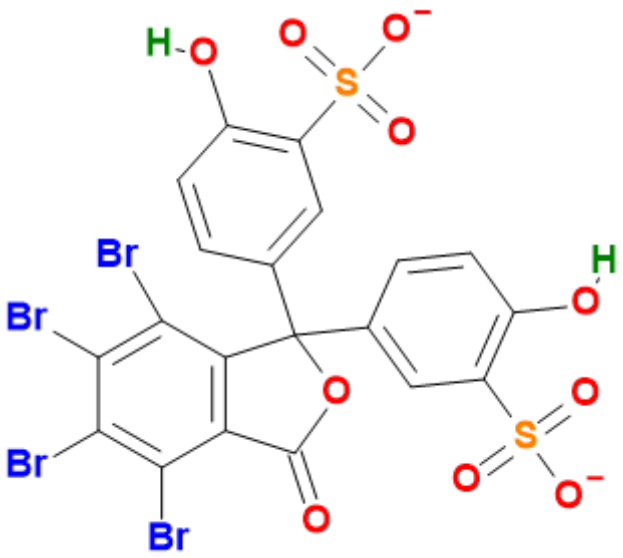


Figure 2.9 The chemical structure of BSP. Generated with BIOVIA Draw 2019. (https://hts.c2b2.columbia.edu/draw/)

2.12 Computational approaches to studying protein-ligand interactions

The increasing cost and inaccessibility of resources have contributed to a bottleneck in the research and development of novel drugs to treat emerging and neglected diseases. Computational biology, including molecular modelling and molecular dynamics (MD) techniques, allow for the optimization and simulation of drug-receptor interactions (Beg et al., 2019). Sophisticated algorithms and energy scoring functions are applied to determine the most stable binding poses, free energies of ligand binding, and key interactions involved in the binding events. These valuable parameters often supplement empirically obtained data to understand the binding behaviour (Safarizadeh and Garkani-Nejad, 2019). Three fundamental steps are involved in molecular docking, pose estimation, virtual screening, and prediction of binding affinities (Guedes et al., 2014).

Different search algorithms apply one of three approaches regarding the protein and ligand flexibilities during pose estimation. 1) The receptor is kept rigid, and certain degrees of freedom of the ligand are investigated.2) The receptor is kept rigid, and all ligand degrees of freedom are investigated.3) The receptor is either moderately or completely flexible, and all degrees of freedom of the ligand are investigated (Guedes et al., 2014). The Glide algorithm used in this study considers the receptor/protein completely rigid during the docking whilst allowing for degrees of freedom in the ligands' rotatable groups. This type of approach is an exhaustive systematic algorithm (Friesner et al., 2004). Scoring functions explore all possible ligand conformations during the docking process, distinguishing empirically obtained poses from those obtained during pose prediction. Most importantly, the binding affinities are effectively estimated and ranked according to stability (lowest binding energies on the energy landscape). Glide uses an empirical scoring function to accurately determine experimental affinity constants from available experimentally obtained structures (de Azevedo and Dias, 2008).

Molecular dynamics of ligand-protein interactions simulate the kinetics of the ligand molecule in and around the protein in the presence of a solvent over a certain time. Thus, providing insights into the motion of the ligand with respect to the protein (Patodia et al., 2014). The top-scoring ligand pose from molecular docking studies is chosen for further analysis by molecular dynamics. Force fields are critical components of molecular dynamics simulation studies. According to (González, 2011) "A force field is a mathematical expression describing the

dependence of the energy of a system on the coordinates of its particles". This provides insights into the system's potential energy with respect to the structures' bonded and non-bonded interactions (Guvench and MacKerell, 2008). Certain parameters, including pressure and temperature, are computed to mimic experimental conditions at the user's discretion. Next, the global energy minima of the protein are computed to attain a state of minimum energy of the structure. The system is then subjected to solvation and equilibration to evenly distribute all energies (kinetic and potential) across the degrees of freedom. Lastly, constraints on the protein are released, and the system is allowed to progress as a function of time (Patodia et al., 2014). In this study, MD methodologies are employed to ascertain key properties of ligand binding between Sj28GST and BSP, including key interactions involved, the binding site of BSP and the stability of this interaction, thus, supplementing experimentally obtained observations.

Chapter 3
Experimental procedures

3.1 Materials

The pET28a (+) vector containing the full-length DNA sequence of Sj28GST with an N-terminal hexahistidine tag was purchased from Gensript (USA). T7-express competent *E. coli* cells were purchased from New England Biolabs (USA). The following reagents were purchased from Sigma-Aldrich (USA): Isopropyl β-D-1 thiolgalactopyranoside, BLUeye prestained protein ladder, Coomasie Blue-G250 dye, Glutathione-agarose resin, L-glutathione, 1-Chloro-2,4-Dinitrobenzene, Praziquantel, Bromosulfophthalein, S-hexyl glutathione, Urea and 8-Anilino-1-naphthalene sulfonic acid. All other reagents utilized were of analytical grade.

3.2 Vector preparation and transformation of host cells

The pET vector system is an efficient expression system for the transcription and expression of target genes using the bacteriophage T7 RNA polymerase regulated by the strong lacUV5 promoter. Expression hosts are lysogens of the λDE3 bacteriophage, containing chromosomal inserts of the T7 RNA polymerase gene, the lacUV5 promoter sequence, and the lacI gene. These features allow for finetuning of expression with the allolactose analogue, isopropyl β-D-1 thiolgalactopyranoside (IPTG). Features of the pET28a (+) vector (Figure 3.1) include a kanamycin resistance gene as a selectable marker, an f1 origin of replication for sequencing and mutagenesis purposes, a C-terminal and N-terminal hexahistidine tag for metal chelation purification as well as a thrombin cleavage site.

The full-length cDNA sequence of Sj28GST with an N-terminal hexahistidine tag was cloned into the pET28a (+) vector (Genscript, USA). To reconstitute the vector, the vial was incubated at room temperature for 30 min at 20 °C then centrifuged (16 000×*g* for 5 min at 20 °C). 100 µL of 0.2 µm filtered Milli-Q® water was added to the vial which was then vortexed for 1 min and centrifuged (16 000×*g* for 10 seconds at 20 °C).

Chemically competent T7-express *E. coli* cells were thawed on ice, and a 50 µL aliquot was mixed with 5 µL of plasmid DNA. The transformation tube was incubated on ice for 30 min followed by a heat shock at 42 °C for 30 seconds to permeabilize the bacterial cell membranes. Cells were then incubated on ice for 5 min, and 950 µL of Super Optimal Broth with Catabolite

repressor (SOC) media (0.5% yeast extract, 2% tryptone, 10 mM NaCl, 2.5 mM KCl, 10 mM $MgCl_2$, 10 mM $MgSO_4$ and 20 mM glucose) was mixed into the tube. The transformed cells were outgrown (37 °C, 220 rpm for 60 min) and plated on 2YT agar selection plates containing 30 µg/mL kanamycin by a serial spread-plate dilution. Selection plates were incubated at 37 °C for 16h.

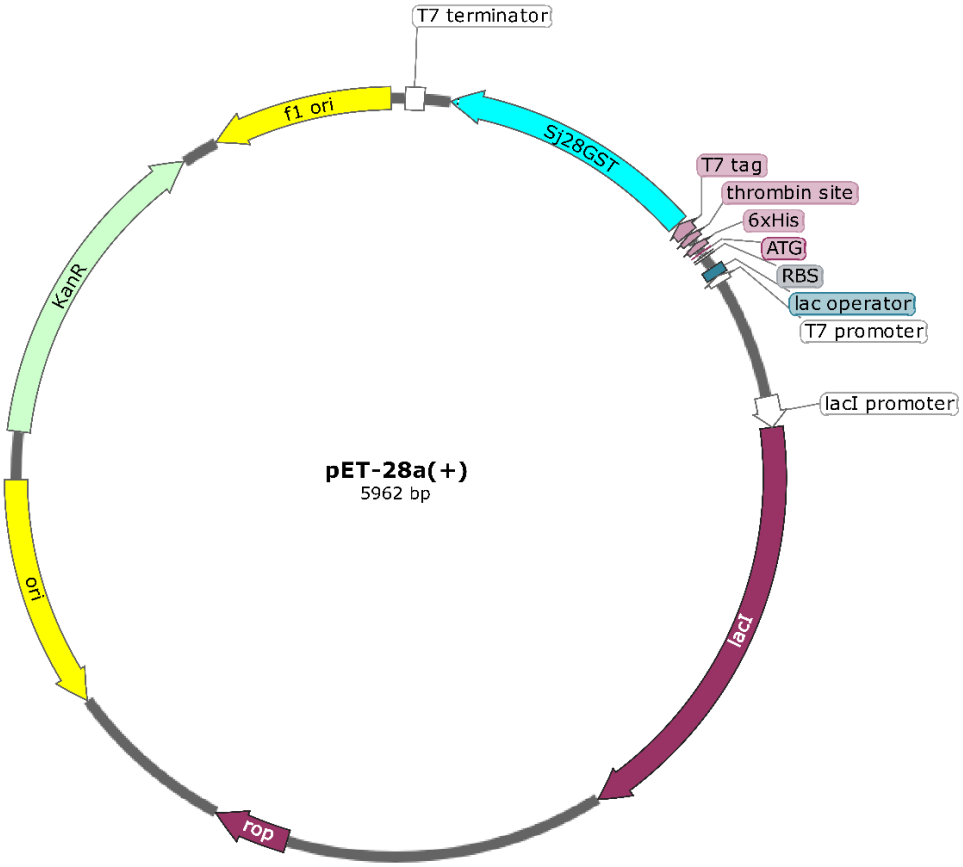


Figure 3.1 A schematic map of the pET-28a (+) vector. The full-length gene sequence of Sj28GST was cloned into the pET-28a (+) vector and only the N-terminal hexahistidine tag was reserved. The vector was synthesised by GenScript® Biotech. Diagram created with SnapGene® Viewer version 4.3.11 (https://www.snapgene.com/snapgene-viewer/)

3.3 Small-scale expression of Sj28GST

A sample induction was carried out to assess the small-scale expression of Sj28GST using 0.5 mM IPTG. Three isolated colonies were selected from transformation plates and each inoculated into 50 mL of 2YT media with 30 µg/mL kanamycin, then incubated overnight (37 °C, 230 rpm for 16h). Dilutions (1 in 50) of the overnight cultures was then prepared in 100 mL of 2YT media with 30 µg/mL kanamycin and incubated (37 °C, 230 rpm) until the mid-exponential phase where OD_{600} = 0.45-0.55 a.u (arbitrary units) was reached. To minimise inclusion body formation, cultures were incubated on ice for 10 min before induction. Cultures were separated into induced and uninduced samples, and IPTG was added to a final concentration of 0.5 mM. Overexpression was then carried out at 30 °C, 250 rpm for 6h. Cells were harvested at 15000×*g* for 15 min at 4 °C and resuspended in ice-cold 1×PBS (Phosphate-buffered saline) then frozen at -80 °C. The small-scale expression of Sj28GST was analysed with SDS-PAGE under reducing conditions. To prepare samples, cell suspensions were thawed and lysed by sonication on ice (5-second pulses, 40 amplitude, 10 times). Then, 1 mL of cell lysates was transferred into microcentrifuge tubes and harvested at 16 000×g for 5 min to separate the soluble and insoluble cell fractions. The insoluble fraction (pellet) was washed three times with Milli-Q® water by sonication and centrifugation. Reducing sample buffer was then added to the fraction samples in a 1:1 ratio.

3.4 SDS-PAGE

SDS-PAGE is a chromatographic technique that allows for the quantitative and qualitative analysis of proteins of interest. By adding the anionic detergent, sodium dodecyl sulphate, to protein samples, charge and shape are cancelled out as mobility variables, allowing proteins to separate solely according to their molecular weights. Under reducing conditions, the purity and homogeneity of expression and purification samples were assessed using glycine SDS-PAGE (Laemmli, 1970).

SDS-PAGE gels (1.5 mm-thick) with a 12.5% separating gel and a 4% stacking gel were prepared from a stock monomer solution of 30% (w/v) acrylamide and 2.7% (w/v) bis-acrylamide, separating [1.5 M Tris-HCl, pH 8.8] and stacking gel buffers [0.5 M Tris-HCl, pH 6.8], 10% SDS and 10% (w/v) ammonium persulfate. Polymerization was catalysed by the addition of tetramethyl-ethylenediamine (TEMED). Reducing sample buffer [12.5% (v/v) 0.5 M Tris 20% (w/v) SDS, 25% (v/v) glycerol, 10% (v/v) b-mercaptoethanol, and 0.5% (w/v) bromophenol blue pH 6.8] was added to samples in a 1:1 ratio which were then incubated in

boiling water for 5 min to ensure complete denaturation. Samples were then centrifuged for 5 min at 5000×*g*, loaded alongside a molecular weight marker and electrophoresed at 160 V for 35 min. Gels were stained with a Coomassie brilliant blue staining solution (0.1% (w/v) Coomassie dye in 1:4:5 ratio (v/v/v) acetic acid-dH_2O-methanol) and de-stained the next day with de-stain solution.

3.5 Large-scale expression of Sj28GST

An overnight starter culture was prepared by inoculating 1 mL of bacterial glycerol stocks of transformed colonies in 50 mL of 2YT media with 30 µg/mL kanamycin grown at 37 °C, 250 rpm for 16h. A 1:100 dilution of the overnight culture was performed in 500 mL of 2YT with 30 µg/mL kanamycin and outgrown at 37 °C, 250 rpm for 2h until mid-exponential phase where the OD_{600} had reached 0.45-0.55 (a.u). Cultures were then incubated on ice for 15 min and induced with 0.5 mM IPTG. Sj28GST was overexpressed at 30 °C, 250 rpm for 6 h. Cells were harvested at 15 000×*g* (4 °C for 15 min), resuspended in ice-cold 1×PBS (Phosphate-buffered saline) and frozen at -80 °C.

For SDS-PAGE analysis of the large-scale expression, various cell-fraction samples were collected. The media fraction was prepared by trichloroacetic-acid precipitation of 1 mL of the media from cell harvesting. The total cell protein fraction was prepared by centrifugation (10 000×g for 1 min at 20 °C) of 1 mL of the cell suspension and resuspension of the pellet in 100 µL of ice-cold 20 mM Tris-HCl pH 8. The soluble(supernatant) and insoluble(pellet) fractions were prepared by centrifugation (16 000×*g* for 5 min at 4 °C) of 1 mL of the cell suspension followed by washing of the pellet three times by centrifugation and sonication.

3.6 Cell lysis and purification of Sj28GST

Frozen cell suspensions were thawed at 20 °C in water. Lysozyme was added to a final concentration of 0.1 mg/mL per 50 mL suspension to facilitate cell lysis. The protease inhibitor, PMSF, was added to a final concentration of 1 mM per 50 mL suspension to minimize proteolysis. The cell suspensions were then mixed by rotation for 20 min at 20 °C. The cells were sonicated on ice at 20-second intervals, 40 amp, six times to ensure complete lysis. Lysed cells were centrifuged (18 000×*g* for 20 min at 4 °C) to produce a clarified supernatant.

Ligand affinity chromatography was utilised to purify Sj28GST from the clarified supernatant. Glutathione agarose affinity chromatography exploits the binding of GST to reduce GSH in the G-site. The matrix consists of immobilized reduced GSH cross-linked to agarose beads.

Bound proteins can then be eluted with excess reduced glutathione or glycine-NaOH to prevent purified protein complex with glutathione. The high binding affinity between GST and its natural ligand, GSH, allows for purifying high yields of pure and active GST under non-denaturing conditions.

A GSH-agarose column was regenerated by cleansing with 5 column volumes of 0.1 M borate buffer, pH 8.5, 5 column volumes of Milli-Q® water with 0.02% NaN_3 and 5 column volumes of 0.1 M acetate buffer pH 4.5 at a flow rate of 4 mL/min. The column was then equilibrated with 10 column volumes equilibration buffer (1×PBS, pH 7.2 with 0.02% NaN_3), and 5 column volumes of the clarified supernatant were pumped through the column twice to maximise binding. Before elution, three wash steps were performed: 10 column volumes equilibration buffer, 10 column volumes equilibration buffer with 0.05% TWEEN®-20 and 10 column volumes equilibration buffer. Sj28GST was then eluted with 5 column volumes of 10 mM glycine-NaOH, pH 10, which was incubated in the column for 10 min to maximise elution. Sj28GST was collected at 1 mL/min and dialysed into a storage buffer (1×PBS, pH 7.2). Samples were collected at each purification step and analysed using SDS-PAGE.

3.7 Quantification of Sj28GST

The concentration of pure Sj28GST was measured by UV-Vis spectrophotometry using a molar extinction coefficient of 14 440 M^{-1} cm^{-1} per monomer (assuming all cysteines are reduced) obtained from the ProtParam online bioinformatics resource portal (Gasteiger et al., 2005). It has been demonstrated that the extinction coefficient of a protein can be accurately determined from the molar extinction coefficients of the tryptophan, tyrosine and cysteine residues in the protein (Gill and von Hippel, 1989). The ProtParam portal computes the molar extinction coefficient of proteins according to the method described by (Pace et al., 1995) where the molar extinction coefficient of a protein at 280 nm in water can be calculated as follows:

$$\varepsilon(M^{-1}cm^{-1}) = 5500(nTrp) + 1490(nTyr) + 125(nCys) \quad (\textit{Equation 4})$$

A two-fold dilution series of purified Sj28GST was prepared using 1×PBS, pH 7.2. Absorbance readings of each dilution were measured at fixed wavelengths of 280 nm (absorption of aromatic amino acids) and 340 nm (scattered light by protein aggregates). The slope of a calibration curve of corrected absorbance (A_{280}-A_{340}) versus the dilution factor was used to calculate the total protein concentration by adaptation of the Beer-Lambert law as follows:

$$[Protein](mg/ml) = \frac{slope \times MW}{\varepsilon \times d} \quad (\textit{Equation 5})$$

Where MW is the molecular weight in Daltons and ε is the molar extinction coefficient in units M^{-1} cm^{-1}

3.8 Far-UV circular dichroism

Far-UV circular dichroism is a spectrophotometric technique used to assess the secondary structural content of biological molecules. The amide backbone of proteins begins to absorb light in the far-UV region, between 200 nm and 250 nm on the electromagnetic spectrum. In Far-UV CD of protein molecules, the differences in the interactions of the peptide backbone with right and left circularly polarized light, in the absence of a magnetic field, provides characteristic CD spectra unique to the secondary structural content of the protein (Fasman, 2013). Alpha-helices display a peak at 190 nm and troughs at 208 nm and 222 nm. Beta sheets display a peak at 195 nm and a trough at 218 nm. Random coils display a peak at 295 and show slight ellipticity at wavelengths greater than 210 nm (Greenfield, 2006).

All cytosolic GSTs are predominantly alpha-helical. This technique was employed to ascertain that overexpressed and purified Sj28GST was correctly folded according to its expected secondary structural composition (Figure 3.2). The Far-UV CD spectrum of a blank and a 5 µM sample of Sj28GST was measured using the Jasco J-1500 CD spectrophotometer between 180 nm and 250 nm at 20°C at a scanning speed of 200 nm/min, data pitch of 0,5 nm, a bandwidth of 2,5 nm and a collection of 5 accumulations per sample. The corrected CD measurement (degrees) was converted into mean residue ellipticity, [θ]mrw to account for the number of absorbing peptide bonds with the following equation:

$$[\theta]_{\mathrm{mrw}} = \frac{\mathrm{MRW} \times \theta_{\mathrm{obs}}}{10 \times \mathrm{l} \times \mathrm{c}}\ \mathrm{deg.\,cm^2.\,dmol^{-1}} \quad (\textit{Equation 6})$$

Where θ_{obs} is the observed ellipticity in degrees. l is the path length in cm. c is the concentration in g/mL. MRW is the mean residue weight which was calculated as follows:

$$MRW = \frac{MW}{n-1} \quad (\textit{Equation 7})$$

Where M is the molecular weight in daltons and n is the number of amino acids.

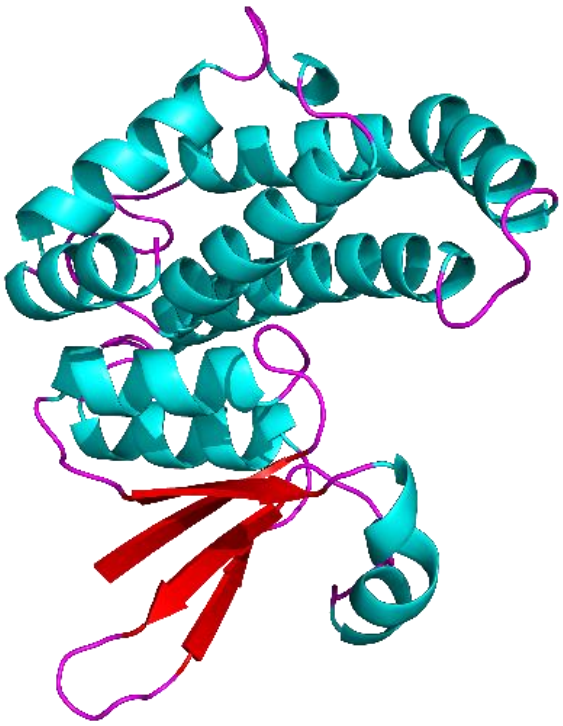


Figure 3.2 A homology model of Sj28GST shown in its monomeric form and coloured according to secondary structure. The protein is predominantly alpha helical, with 4 antiparallel beta strands (red) and 8 alpha helices (cyan). Generated using the Pymol molecular graphics programme.

3.9 Extrinsic ANS fluorescence

Extrinsic fluorescence was applied to ascertain the binding of BSP to Sj28GST. 8-anilino-1-naphthalene sulfonate (ANS) (Figure 3.3) is a hydrophobic fluorophore used to probe for binding to buried hydrophobic surfaces on protein molecules. Upon localization to non-polar, hydrophobic environments, there is a change in the molecule's excited state, resulting in an increased fluorescence quantum yield accompanied by a hypsochromic (blue) shift relative to unbound polar-solvent exposed ANS (Stryer, 1968). Three main hydrophobic pockets exist in the Sj28GST dimer where ANS can bind, the G-site, the H-site and the cleft at the dimer interface. If BSP has a higher affinity to the ANS-binding sites on Sj28GST, the drug may displace the fluorophore, decreasing the observed quantum yield. Although the exact binding sites cannot be ascertained from this technique, ANS displacement studies serve as a useful tool to confirm the binding of the drug to hydrophobic patches, especially in the case where intrinsic fluorophores such as tryptophan residues are minimal in the amino acid sequence.

To begin the reaction, 500 µL samples were prepared in PBS buffer, pH 7.2 with 1 mM EDTA. 400 µM of ANS was selectively exited at 390 nm in the presence and absence of 200 µM BSP and 10 µM Sj28GST. Fluorescence emission spectra were collected from 400 to 600 nm using the Jasco FP-6300 Spectrofluorometer. Experiments were repeated with a buffer containing 1 mM GSH and 1 mM of the product analogue, s-hexylglutathione (GTX). GSH and GTX-containing experiments were carried out to block either the G-site (GSH) or both the G and H-site (GTX).

All emission spectra were corrected for the fluorescence of free-unbound ANS. A BSP sample was also excited to ensure that the drug showed no background fluorescence at the studied wavelengths. Samples containing BSP were corrected for the absorption of light by the drug at the excitation and emission wavelengths, known as the primary and secondary inner-filtering effects using the following equation described by (Lakowicz, 2013).

$$F_{corr} = F_{obs} \times 10^{\frac{OD_{ex}+OD_{em}}{2}} \quad (\textit{Equation 8})$$

Where F_{corr} and F_{obs} are the corrected and observed fluorescence emission intensities and OD_{ex} and OD_{em} are the optical densities at the excitation and emission wavelengths.

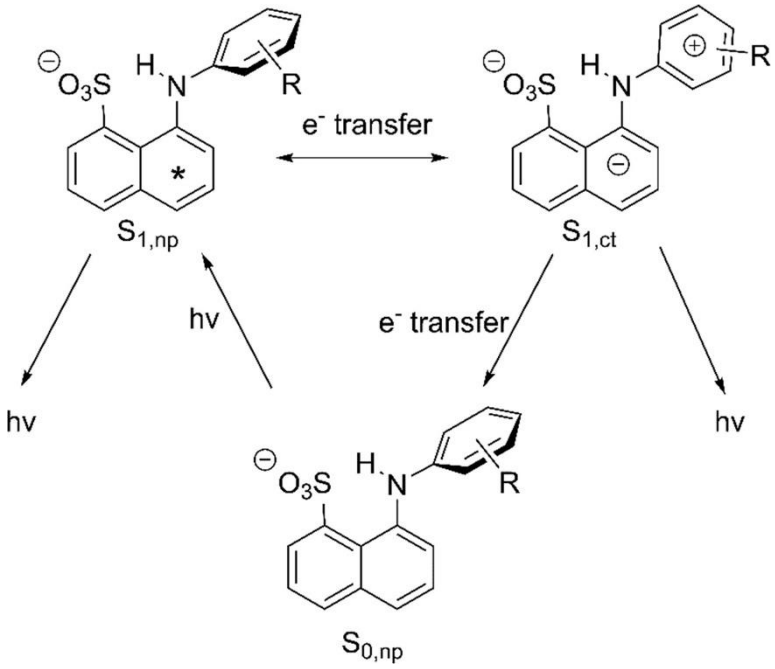


Figure 3.3 8-anilino-1-naphthalene sulfonate (ANS). In non-polar environments, excitation is localized around the naphthalene ring, resulting in a state known as the non-polar (np)state. Upon exposure to more polar environments, the initial high energy non-polar state interacts with the polar solvent to orient the polar dipoles, resulting in the emission of a photon and a shift to a lower-energy; longer wavelength state known as the charge-transfer (ct) state. Adapted from (Wang et al., 2019)

3.10 Steady-state kinetic studies

The activity of purified GST can be determined using the spectrophotometric analysis of CDNB (1-Chloro-2,4-dinitrobenzene) conjugation to GSH (Figure 3.4). The formation of a thioether bond between the thiol group on the glutathione cysteine and CDNB results in a measurable colour change at 340 nm (Habig and Jakoby, 1981). The CDNB-GSH conjugation activity assay was performed to determine the following steady-state kinetic parameters in the presence and absence of BSP, specific activity, V_{max}, K_M, and k_{cat}/K_M as the half-maximal inhibitory concentration (IC_{50}) of BSP. All data were fitted using the GraphPad Prism software, version 8.0.2 (https://www.graphpad.com/).

To determine the specific activity, 2900 µL of reaction buffer (100 mM NaH_2PO_4 containing 0.02% (w/v) NaN_3, 5 mM DTT and 1 mM EDTA, 1mM GSH) was added to a 3 mL quartz cuvette (10 mm path length) to which 100 µL of 30 mM CDNB in ethanol was added to the reaction mix to reach a final concentration of 1 mM. This was performed at varying Sj28GST concentrations (8.25 nM - 42.5 nM). The Steady-state kinetic assays were performed by adding 100 µl of varying concentrations of GSH or CDNB to 2900 µL of reaction buffer containing 100 nM of Sj28GST and 1 mM GSH/CDNB. V_{max} and K_M were determined from a non-linear regression, Michaelis Menten plot with the following model:

$$V_0 = \frac{V_{max} \times [S]}{K_M + [S]} \quad (\textit{Equation 9})$$

Where V_0 is the initial velocity in µmol/min and [S] is the substrate concentration in mM.

The catalytic efficiency (k_{cat}/K_M) was obtained from the slope of a linear plot of substrate concentration versus activity where the substrate concentration is much lower than the K_M according to the following adaptation of the Michaelis-Menten equation:

$$V_0 = \frac{k_{cat}}{K_M} [E][S] \quad (\textit{Equation 10})$$

Where V_0 is the initial velocity in µmol/min, [E] is the total enzyme concentration in mM and S is the substrate concentration (GSH or CDNB) in mM

Lastly, an inhibitor series was prepared and assayed to determine BSP's half-maximal inhibitory concentration (IC50) towards Sj28GST. 2900 µL of reaction buffer containing 25 nM Sj28GST and 1 mM GSH at varying BSP concentrations (0-5 mM) was assayed with the addition of 100 µL of a CDNB stock solution. The data were fitted using the following non-linear regression model with a four-parameter variable slope:

$$Y = \frac{Bottom+(Top-Bottom)}{(1+10^{((LogIC50-X)\times Hillslope)}} \quad (Equation\ 11)$$

Where X is the Log of inhibitor concentration in µM, and Y is the % activity. Top and Bottom are the graph plateaus with the same units as Y. $LogIC_{50}$ is in µM, and Hillslope is the slope factor.

The linear appearance of the product was measured over 60 s with the Jasco V-630 UV/Vis spectrophotometer using the time course measurement application at 340 nm.

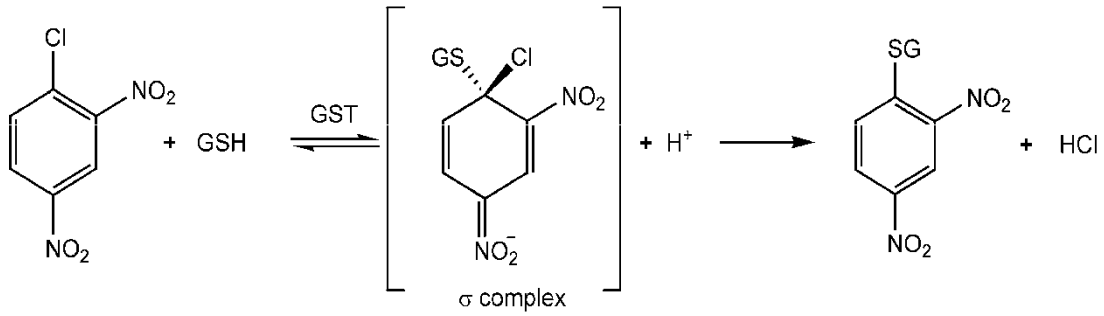


Figure 3.4 A scheme of the CDNB-GSH conjugation assay. Adapted from (Bocedi et al., 2019)

3.11 Isothermal titration calorimetry

All ITC experiments were performed on the standard volume Nano ITC (TA Instruments Inc., Delaware, USA). 60 µM of Sj28GST was dialysed overnight into the reaction buffer (1× PBS with 1 mM TCEP and 2 mM EDTA, pH 6.5) in the presence or absence of 1 mM GSH. A working stock of 1.09 mM BSP was then prepared in the dialysate from a stock solution of 109 mM in 100% (v/v) DMSO. DMSO was added to the protein sample to a final concentration of 1% (v/v) to prevent buffer mismatches between the protein and ligand sample. All solutions (protein, ligand and buffer) were degassed for 20 min at 0.3-0.5 atm before running the experiments. The reference cell was filled with Milli-Q® water, and the sample cell was filled with 1.5 mL of the protein sample (effective volume: 1.2 mL). A 250 µL injector syringe was filled with the ligand sample, leaving a 5-10 µL air bubble between the plunger and the solution to avoid signal distortion. Incremental titrations were performed at 25 °C, a stirring rate of 250 rpm with 50 injections of 5 µL each and 300 seconds between each injection. Ligand into buffer titrations was performed to correct for heats of dilutions. All data analysis and corrections were conducted using the NanoAnalyze data analysis software (TA Instruments Inc., Delaware, USA). The baseline and heats of dilution-corrected data were fitted using an independent binding model.

3.12 Urea-induced equilibrium studies

A stock solution of 10 M urea was prepared using the previously described method (Pace and Scholtz, 1997) in 20 mM sodium phosphate buffer, pH 6.5. Briefly, the final concentration of the prepared urea stock solution was confirmed using the methods of measured weights and refractive indexes. Equilibrium-unfolding and refolding experiments were performed at 20°C in 20 mM sodium phosphate containing 1 mM DTT and 1 mM EDTA, pH 6.5.

To determine the concentration of urea required to fully unfold the protein after a certain incubation period, 1 µM of protein sample was incubated in varying concentrations of urea (0-8 M), and the tryptophan fluorescence signal of the unfolding samples was measured every 20 min until there was no change in the signal. Signals were measured again after 24h to confirm that the samples were completely unfolded.

Reversibility studies were performed to ensure that the unfolding and refolding paths were in equilibrium. Unfolding and refolding samples of 1 µM protein were prepared in varying urea concentrations as summarised in Table 1. Samples were then incubated, and the tryptophan fluorescence signal was measured until the signals of the unfolding and refolding samples were

identical within a margin of error. Equilibrium-unfolding and refolding experiments were then performed at the established urea concentration (6 M for 1h) and equilibrium time (> 4h).

Tryptophan fluorescence was used as a structural probe to monitor the unfolding pathway. The lone tryptophan on Sj28GST was selectively excited at 295 nm, and fluorescence emission scans were taken from 295 nm to 450 nm. The CDNB-GSH conjugation assay was used as a functional probe to follow the unfolding pathway. Unfolding and refolding samples were assayed in reaction buffer containing 1 mM GSH and 1 mM CDNB, the final protein concentration was 33.3 nM.

The urea denaturation curves were generated according to a two-state folding pathway where the unfolded and folded conformations are highly populated at equilibrium (Pace and Scholtz, 1997) so that the sum of the fractions of folded and unfolded proteins equals one:

$$f_f + f_u = 1 \quad \textit{(Equation 12)}$$

Where f_f and f_u are the fractions of the folded and unfolded conformations respectively.

Therefore, y for any point on the denaturation curve, which corresponds to the signal measured to follow unfolding is described by:

$$y = y_f f_f + y_u f_u \quad \textit{(Equation 13)}$$

The fraction of unfolded protein can thus be determined from a combination of the two equations where:

$$f_u = (y_f - y)\,(y_f - y_u) \quad \textit{(Equation 14)}$$

The equilibrium constant (K_{eq}) and Gibbs change in free energy (ΔG) for the unfolding pathway can then be calculated as follows:

$$K_{eq} = \frac{f_u}{f_g} = \frac{f_u}{1-f_u} = \frac{y_f - y}{y - y_u} \quad \textit{(Equation 15)}$$

And

$$\Delta G = -RT ln K_{eq} \quad \textit{(Equation 16)}$$

Table 1: Summary of unfolding and refolding samples set-up

Final [Urea] (M)	Urea (µL)	Buffer (µL)	Native Protein (µL)	Urea (µL)	Buffer (µL)	Unfolded Protein (µL)
	Unfolding			Refolding		
0	0	950	50	-	-	-
0.5	50	900	50	0	937.5	62.5
1	100	850	50	50	887.5	62.5
1.5	150	800	50	100	837.5	62.5
2	200	750	50	150	787.5	62.5
2.5	250	700	50	200	737.5	62.5
3	300	650	50	250	687.5	62.5
3.5	350	600	50	300	637.5	62.5
4	400	550	50	350	587.5	62.5
4.5	450	500	50	400	537.5	62.5
5	500	450	50	450	487.5	62.5
5.5	550	400	50	500	437.5	62.5
6	600	350	50	550	387.5	62.5
6.5	650	300	50	600	337.5	62.5
7	700	250	50	650	287.5	62.5
7.5	750	200	50	700	237.5	62.5
8	800	150	50	750	187.5	62.5

Calculations based on a 10 M urea stock; 20 µM native protein stock for unfolding samples and a 16 µM unfolded protein stock in 6M urea for refolding samples. The final protein concentration is 1 µM.

Chapter 4
Computational Procedures

4.1 Molecular docking of ANS and BSP on Sj28GST

A homology model of Sj28GST was generated using the SWISS-MODEL protein structure homology modelling server on Expasy (Waterhouse et al., 2018). The template structure corresponding to Sh28GST (PDB ID: 1OE8) shows 77% sequence homology to Sj28GST, and the predicted model was validated using the PROCHECK tool on the PDBsum server (Laskowski et al., 1997). Before induced-fit ligand docking on the Schrodinger Maestro V12.2 algorithm, the protein and ligands were subjected to a series of preparation and optimization steps. Firstly, the two GSH ligands on the PDB file of the predicted model of Sj28GST were removed, and the following operations were applied to the structure: assigning of bond orders, the addition of hydrogen atoms, assigning of zero bond orders to disulfides and metal groups and the removal of waters within 5 Å distance from heteroatoms. The PROPKA algorithm was used to assign water molecules to a pH of 7. The structure was then energy minimised with the OPLS_2005 force field with an RMSD cut-off of 0.3 Å. The ANS and BSP structure files were obtained from the PubChem database (https://pubchem.ncbi.nlm.nih.gov/) and prepared using the LigPrep tool in Maestro. Ligand preparation involved desalting the ligands, producing probable tautomeric states and chiral centre restraining where multiple chiral centres were present. Induced fit ligand docking was then performed in Maestro and the entire protein dimer was set as a binding site due to the presence of three possible binding sites, namely the G-site, H-site and the narrow cleft at the enzyme's dimer interface. The top-scoring pose (lowest glide score and glide emodel) were selected for molecular dynamics simulations. Glide scores approximate the empirical free-energy of the ligand-binding event. Therefore, lower glide scores are indicative of higher-affinity, more stable binding interactions.

4.2 Molecular dynamics simulations

Molecular dynamics simulations of the highest-scoring ANS and BSP poses on the Apo Sj28GST molecule were carried out using the Desmond programme applied in Schrodinger Maestro V12.2. The systems were solvated in an explicit solvent with the OPLS_2005 force field. The system was then subjected to energy minimization, which was followed by neutralization. Neutralization involves the placement of counter-ions within a 20 Å distance

from the ligand molecule and the addition of chlorine and sodium ions by computationally conditioning the system environment to 0.15 M NaCl. Lastly, equilibration of all potential and kinetic energy forces in the system was performed in seven short consecutive runs. Runs one and three were performed under NVT (Constant number of particles, volume and temperature) conditions at 10 K and stages 4-6 were performed under NPT (Constant number of particles, pressure and temperature) conditions at 10 K. The final production dynamics 50 ns simulation stage was carried out at 300 K at constant pressure. Post-production dynamics analysis and visualisation were carried out in Schrodinger Maestro (Simulation Interaction Diagram and Simulation Events Analysis algorithms) and the PyMol molecular graphics programme. The following important terms were obtained from the simulation analysis: 1) The total average energy of the structure over time, 2) The root means square deviation (RMSD) of the alpha carbons, 3) The root mean square fluctuation (RMSF) of the alpha carbons as well as the ligand with respect to the protein and 4) The radius of gyration (Rg).

Chapter 5
Experimental Results

5.1 Small-scale expression

Small-scale expression was carried out to assess the overexpression of Sj28GST using 0.5 mM IPTG at 30°C for 6h. The conditions were chosen based on the needs previously used for the expression of Sj26GST. Figure 5.1A shows SDS-PAGE expression analysis from three isolated colonies on a 12.5% gel. The gel indicates the expression of Sj28GST by transformed T7 cells into the soluble fraction (supernatant).

5.2. Large-scale expression and purification

Sj28GST was overexpressed on a larger scale following induction trials (Figure 5.1A) to improve protein yields. Various cell fractions were electrophoresed on an SDS-PAGE gel to ensure no protein was lost during the cell harvesting/lysis steps (Figure 5.1B). The gel shows that most of the protein is populated in the supernatant. There is a faint band of protein in the pellet, which may have resulted from insufficient washing of the pellet sample during fractionation. Pure Sj28GST was obtained using glutathione-agarose affinity chromatography by elution with glycine-NaOH. The appearance of a single distinct band in collected fractions indicates pure Sj28GST (Figure 5.1C). A faint higher molecular weight band can be seen in lanes with higher-intensity bands, which correspond to the enzyme's dimeric form (56 kDa). This may have been a result of incomplete denaturation during sample preparation.

A standard curve of the protein molecular weight ladder was generated to estimate the molecular weight of the purified protein fractions (Figure 5.1D). Relative migrations were plotted against the log of molecular weight and interpolated to estimate the protein size. From the standard curve, the estimated protein size is 28.4 kDa which corresponds with the expected molecular weight of the protein. The standard curve shows a strong linear relationship between the two variables ($R^2 = 0.95$), demonstrating that the protein's molecular weight was reliably predicted.

5.3. Quantification and purity assessment

Purified Sj28GST was quantified spectrophotometrically using the Beer-Lambert law (Equation 5). A serial dilution of purified protein was prepared, and the absorbance of each

sample was measured at 280 nm, which was corrected for aggregation at 340 nm. The slope of a standard curve of absorbance versus concentration was then used to calculate the concentration (37 µM) (Figure 5.2A). A UV scan of 1 in 50 dilutions in 1×PBS, pH 7.2 of purified Sj28GST was measured to assess its purity (Figure 5.2B). A single, sharp peak at 280 nm represents the absorption of light by the aromatic residues: tryptophan and tyrosine. The very low absorbance at higher wavelengths, particularly at 340 nm, indicates no light scattering by protein aggregates. Lastly, the 260/280 ratio is 0.64, which is ideal for pure protein samples and indicates the absence of any nucleic acid contamination.

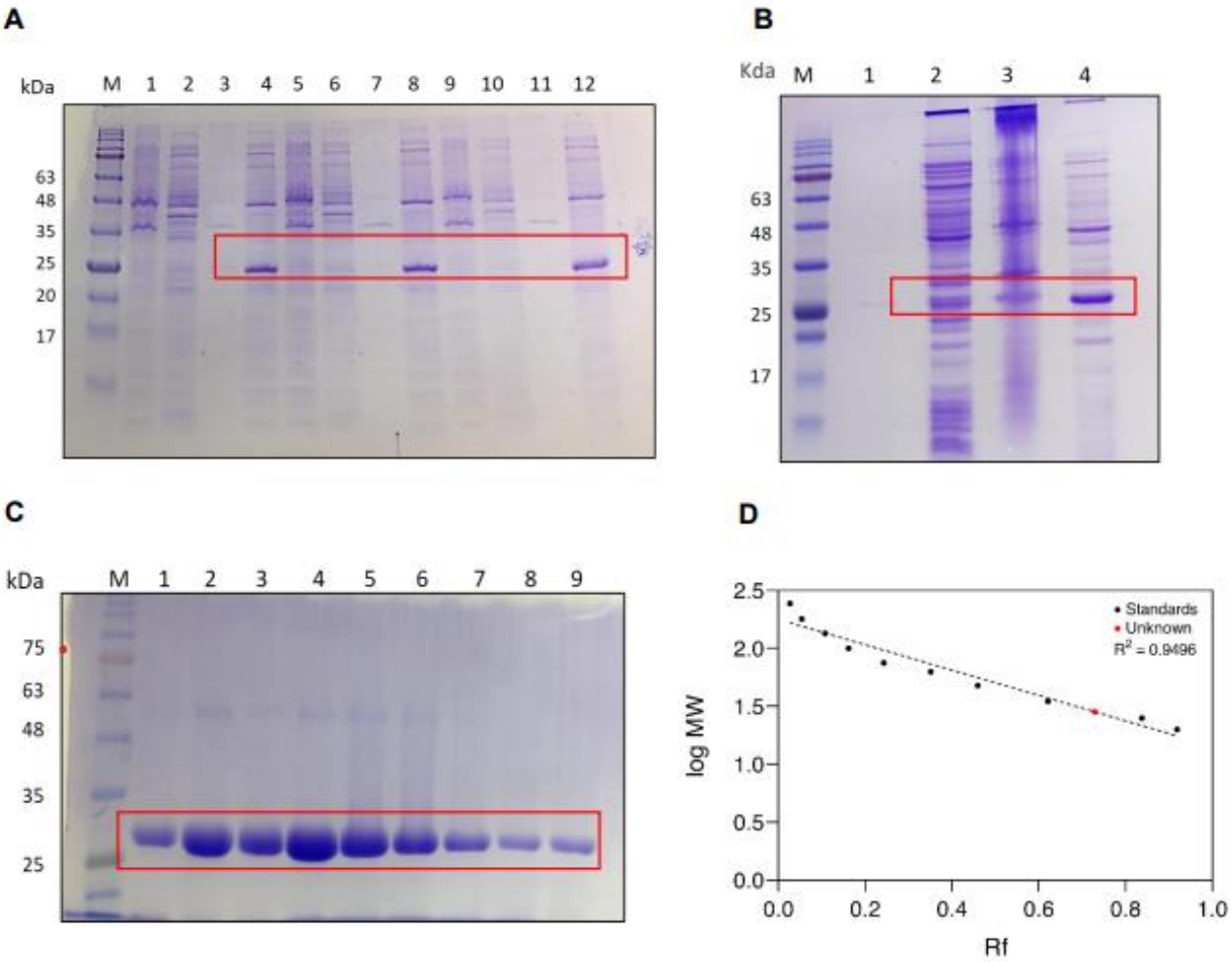


Figure 5.1 SDS-PAGE analysis of Sj28GST (red box) overexpression **A.** Small-scale induction trials of expression conditions for three isolated colonies. Lanes 1,2,5,6,9,10: uninduced, Lanes 3,4,7,8,11,12 induced using 0.5 mM IPTG at 30°C for 6h. Pellet samples are in odd lanes; supernatant samples are in even lanes **B.** Analysis of various fractions of large-scale overexpression. Lane 1: Media sample, Lane 2: Cell lysate, Lane 3: Pellet, Lane 4: Supernatant . **C.** Various fractions of purified SJ28GST using glutathione-agarose affinity chromatography. Faint bands appear at ~ 56 kDa for high intensity samples which represent the dimeric form due to incomplete denaturation of samples. **D.** Standard curve for estimation of purified Sj28GST molecular weight. The estimated molecular weight according to relative migration distances is 28.4 kDa

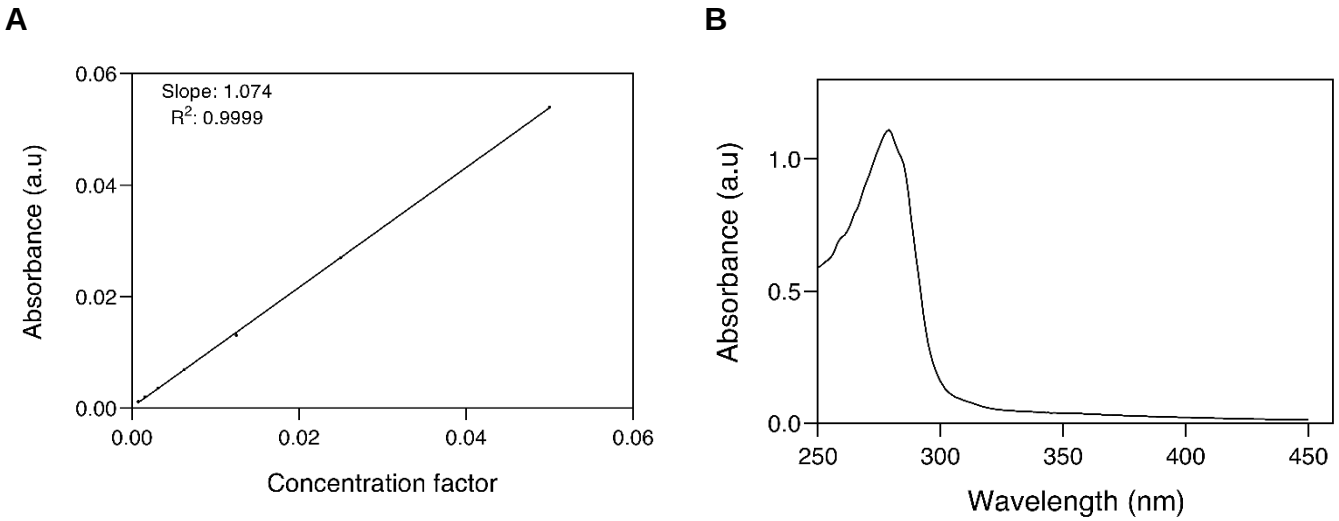


Figure 5.2 Quantification and spectral properties of purified Sj28GST, **A.** The concentration of purified Sj28GST was quantified by plotting a standard curve of various dilutions. The absorbance of each dilution was measured at 280 nm and corrected for any light scattering by protein aggregates at 340 nm. The concentration was calculated from the slope and the protein's molar extinction coefficient to be 37 µM. **B.** The UV spectrum of purified Sj28GST was measured to assess the purity of the protein sample. The peak at 280 nm represents absorption by aromatic residues and the absence of a peak at 340 nm indicates that there is no significant aggregation. The A_{260}/A_{280} ratio of 0.64 indicates no nucleic acid contamination.

5.4 Far-UV Circular dichroism

The Far-UV CD spectrum of Sj28GST was measured to confirm that the purified protein was folded in its expected conformation by monitoring its secondary structure (Figure 5.3). The Far-UV CD spectrum of a 5 µM protein sample showed troughs at 208 nm and 222 nm and a peak at 195 nm. These characteristics confirm that the protein is predominantly alpha-helical, characteristic of cytosolic GSTs.

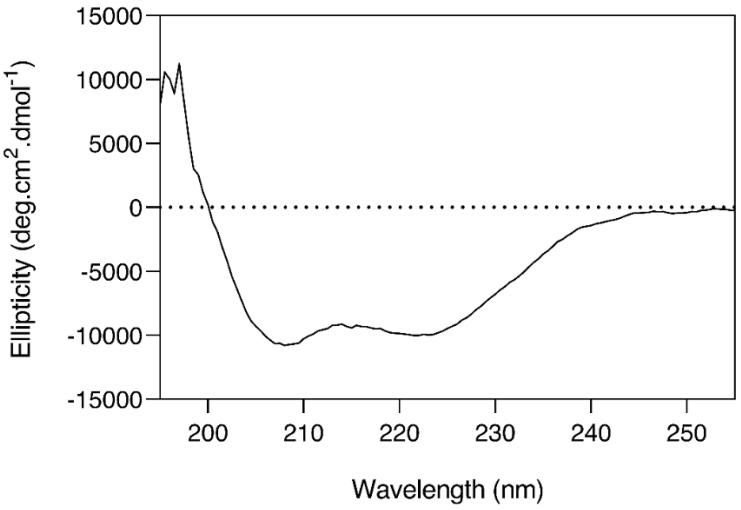


Figure 5.3 Far-UV CD spectrum of Sj28GST. A 5µM sample was prepared in 1×PBS, pH 7.2. The blank-corrected spectrum was converted into mean residue ellipticity to account for the number of peptide bonds. The spectrum shows troughs at 208 and 222 nm, which is characteristic of a predominantly alpha-helical protein.

5.5 Extrinsic ANS fluorescence

ANS was used as an extrinsic probe for the presence of hydrophobic binding sites on the Sj28GST surface (Figure 5.4). ANS samples (400 µM) were selectively exited at 390 nm in the presence and absence of 200 µM BSP and 10 µM Sj28GST. Samples containing only protein display an increased fluorescence emission relative to free ANS. This is coupled by a blue shift to shorter wavelengths (518 nm – 487 nm), suggesting that the ANS excited state shifts to the non-polar, high-energy state due to binding to non-polar/hydrophobic surfaces on Sj28GST. The introduction of BSP significantly decreased the quantum yield (68%), suggesting a displacement of ANS by the BSP molecules. The signals are identical in the presence of excess (1 mM) GSH and GTX, showing that BSP continues to bind and displace ANS despite the unavailability of the G-site and H-site. A 200 µM BSP sample was also excited at 390, and the fluorescent emission scan shows that the molecule does not contribute any background fluorescence to the ANS spectra.

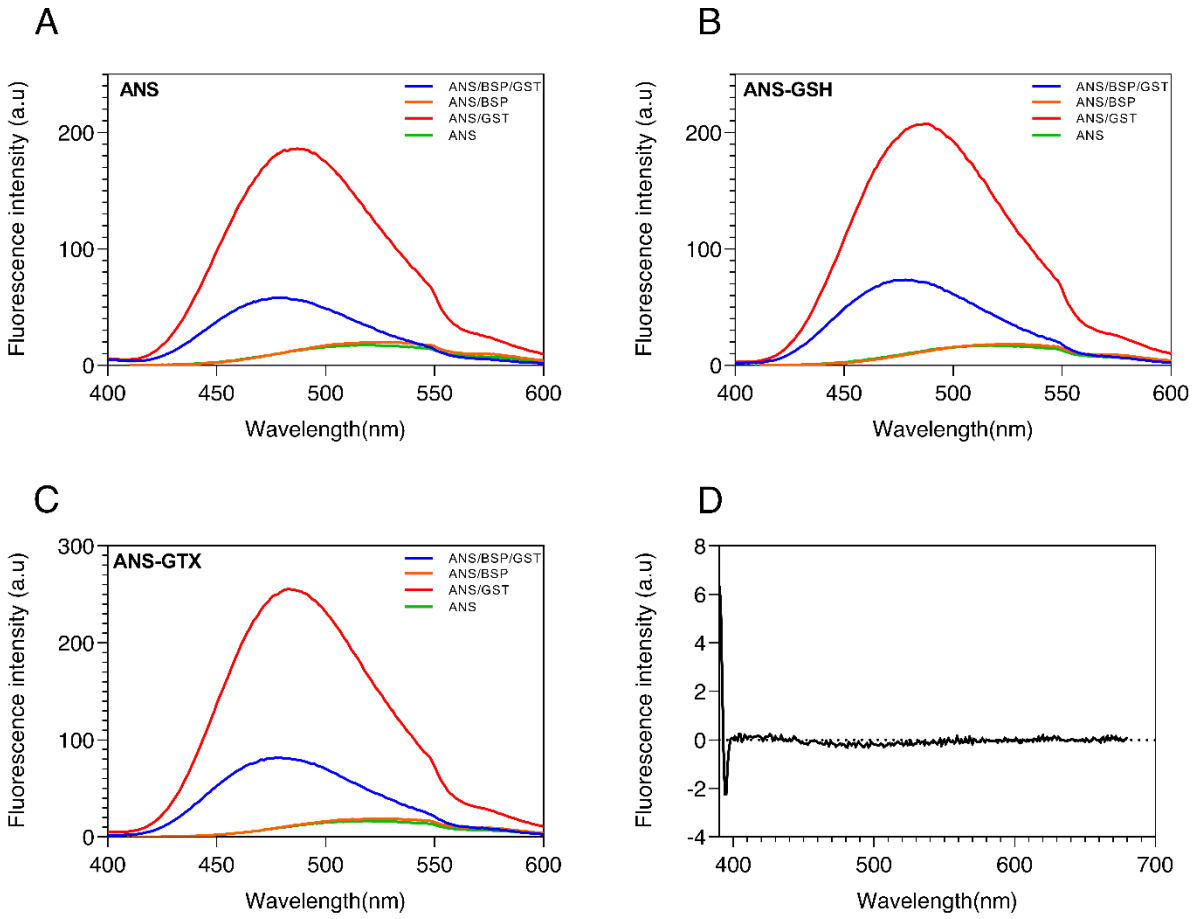


Figure 5.4 Extrinsic ANS fluorescence of BSP binding to Sj28GST. Extrinsic fluorescence of ANS only (green), ANS with Sj28GST(red), ANS with BSP (orange) and ANS with BSP and Sj28GST(blue). **A.** Fluorescence spectrum measured in buffer only (1×PBS containing 1 mM EDTA, pH 7.2). **B.** Fluorescence spectrum measured in buffer containing 1 mM glutathione. **C.** Fluorescence spectrum measured in buffer containing 1 mM s-hexylglutathione. **D**. Fluorescence scan of BSP showing no background fluorescence of the drug.

5.6 Steady-state kinetic studies

The steady-state kinetic parameters for Sj28GST were determined in the presence and absence of BSP using the CDNB-GSH conjugation assay. These results are summarised in Table 2. The specific activity is almost completely flattened (99%) in the presence of 0.5 mM BSP. The K_M, V_{max} and catalytic efficiency (k_{cat}/K_M) towards GSH are decreased by 58%, 46%, and 60% respectively in the presence of 0.84 µM BSP, which indicates uncompetitive inhibition of activity. Lineweaver-Burk double reciprocal plots in increasing BSP concentrations also yielded parallel lines, characteristic of competitive inhibition. The Michaelis-Menten kinetic parameters towards CDNB in BSP presence could not be detected as the enzyme did not reach saturation at higher CNDB concentrations assayed. Therefore, the mode of inhibition of the drug towards the H-site couldn't be accurately determined from the non-linear regression fit (Figure 5.6).

The IC_{50} of BSP towards Sj28GST activity was also determined using the CDNB-GSH conjugation assay. A 25 nM protein sample was assayed at varying concentrations of BSP, and the data were fitted using a non-linear regression model with a four-parameter variable slope (Figure 5.5). The IC_{50} value obtained is in the µM range (0.75 µM).

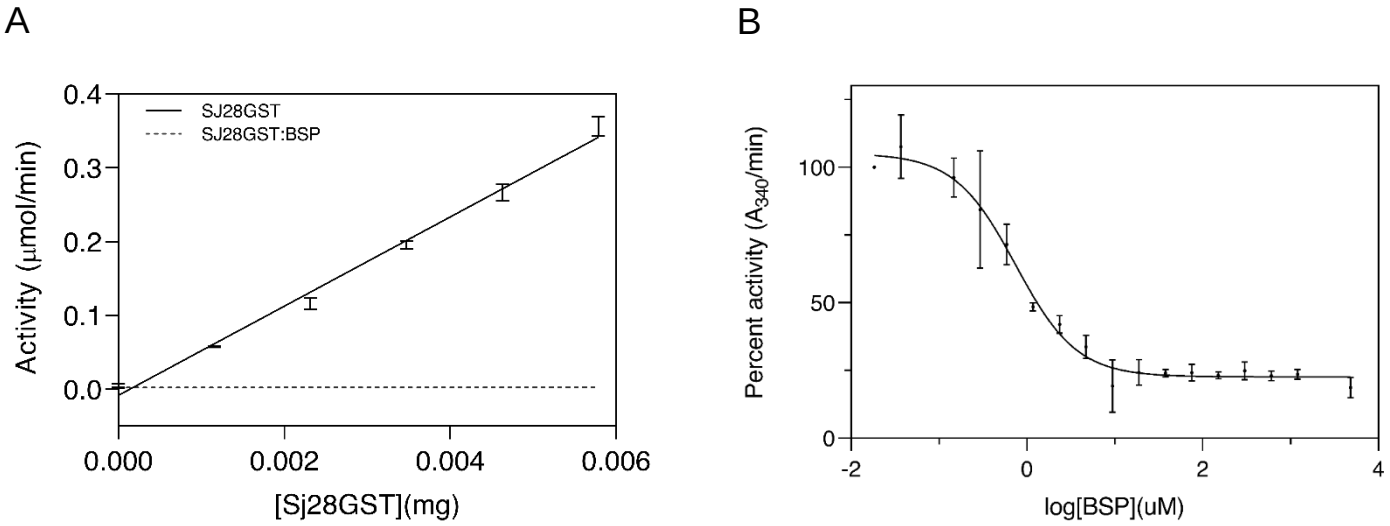


Figure 5.5 Specific activity and IC_{50} studies of BSP on Sj28GST activity. **A.** Varying Sj28GST concentrations were assayed in the presence (dotted line) and absence (solid line) of 0.5 mM of BSP using the CDNB-GSH conjugation assay. All assays were performed in triplicates and the data was corrected for non-enzymatic rates. The obtained slopes were 60.04 and 0.0742 which correspond to the specific activity (µmol/min/mg) in the presence and absence of BSP respectively. **B.** The CDNB-GSH conjugation assay was performed at varying BSP concentrations (0-5 mM) in the presence of 25 nM protein. The observed IC_{50} from a non-linear regression model with a four-parameter variable slope was 0.75 µM (±0.09). The fit displays a hillslope of -1.24 with an R^2 of 0.96.

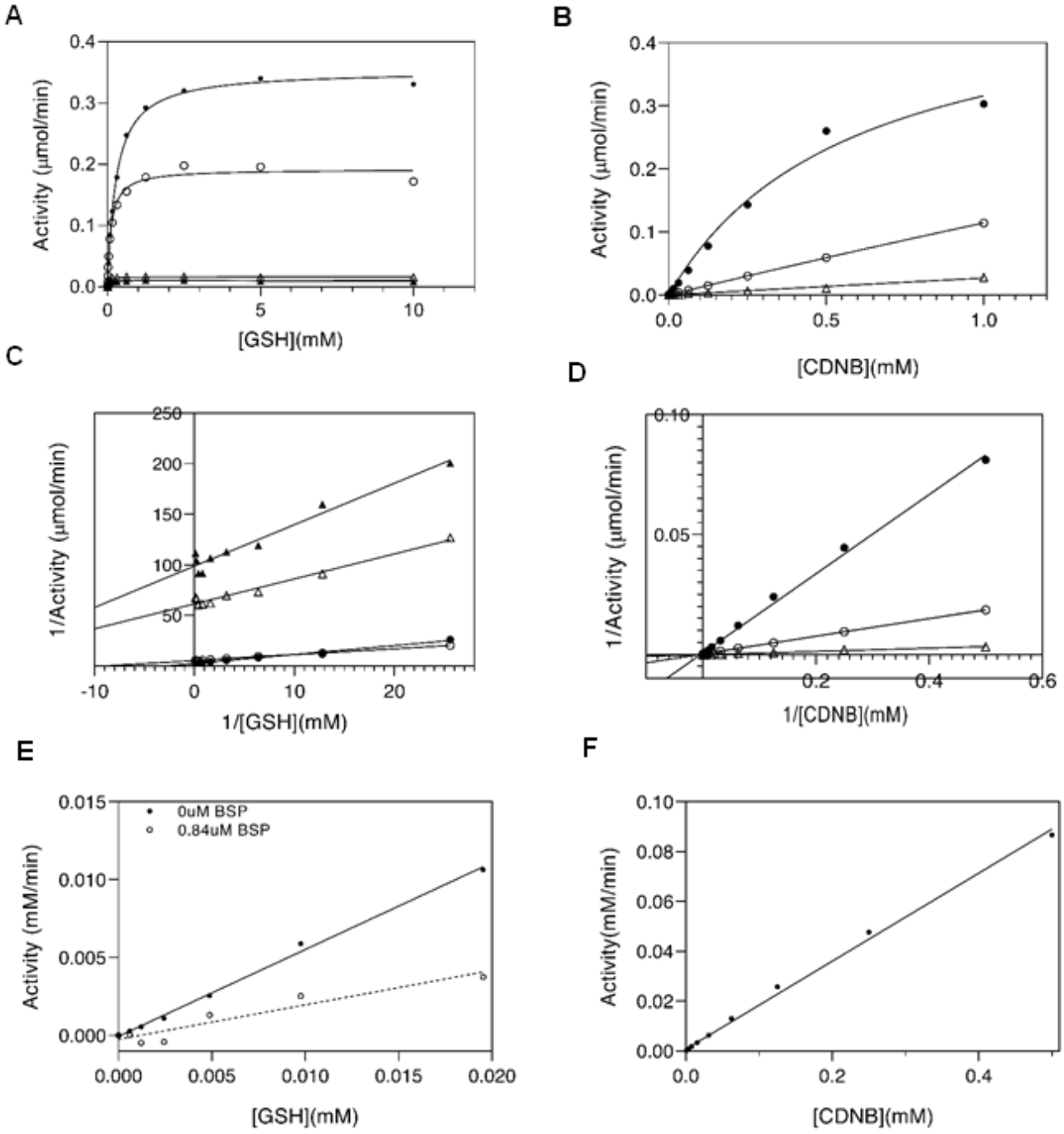


Figure 5.6 Summary of the effects of BSP on the steady-state kinetic parameters of Sj28GST**. A.** Michaelis-Menten plot of 100 nM Sj28GST towards GSH in the presence of 0 µM (●), 0.84 µM (○), 4.2 µM (Δ) and 8.4 µM (▲) BSP. **B**. Michaelis-Menten plot of 100 nM Sj28GST towards CDNB in the presence of 0 µM (●), 0.84 µM (○) and 4.2 µM BSP. **C**. Lineweaver-Burke plot of steady-state kinetics towards GSH. **D**. Lineweaver-Burke plot of steady-state kinetics towards CDNB. **E**. Linear plot of GSH concentration against activity at concentrations lower than the K_M for the determination of the catalytic efficiency in the presence (dotted line) and absence (solid line) of BSP the slopes (0.2214, R2=0.903µ8) and (0.5574, R2=0.996) were used to determine the catalytic efficiency in s-1 M-1**. F.** Linear plot of CDNB concentration against activity at concentrations lower than the Km for the determination of catalytic efficiency in the absence of BSP the slope (0.1767, R2=0.9967) was used to determine the catalytic efficiency in s-1 M-1.

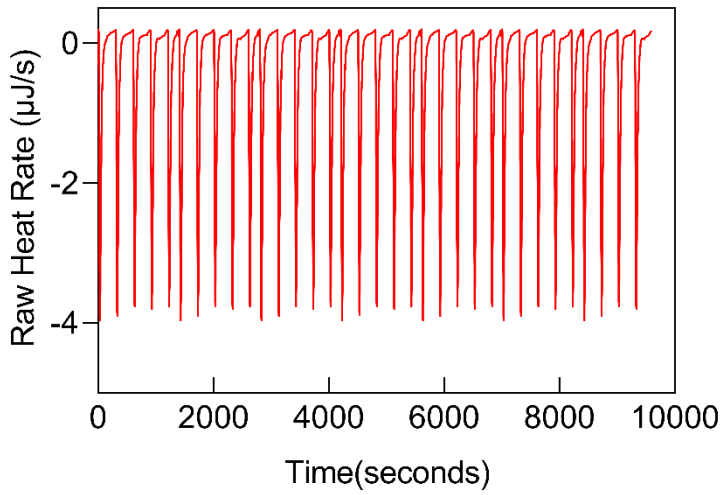
Table 2: Kinetic parameters of Sj28GST in the presence and absence of BSP

	No inhibitor	With BSP
Specific activity (CDNB)		
µmol min^{-1} mg^{-1}	60.4 ± 1.82	0.0742 ± 0.03[a]
Towards CDNB		
K_M (mM)	0.587 ± 0.04	ND
V_{max} (µmol min^{-1})	0.533 ± 0.02	ND
k_{cat}/K_M (s^{-1} M^{-1})	29 450	ND
Towards GSH		
K_M (mM)	0.285 ± 0.01	0.120 ± 0.01[b]
V_{max} (µmol min^{-1})	0.353 ± 0.004	0.192 ± 0.004[b]
k_{cat}/K_M (s^{-1} M^{-1})	92 900	36 833[b]

ND: Not detected (enzyme does not reach saturation)
[a] Assays performed in the presence of 0.5 mM BSP
[b] Assays performed using 0.84 µM BSP

5.7 Thermodynamics of Sj28GST: BSP binding: ITC

ITC experiments were carried out to determine the driving forces of BSP binding to Sj28GST. A 60 µM protein sample was titrated with 5 µL incremental titrations of 1.09 mM BSP until saturation was reached. The experiment was repeated in the presence of 1 mM GSH. The binding isotherms were corrected for heats of dilutions, which correspond to the average areas of the final ten injections. Both isotherms demonstrate sigmoidal curves with exothermic reactions (Figure 5.7). Figure inserts summarize the thermodynamic parameters obtained from the data fitting to an independent model using the Nanoanlyze software (TA Instruments Inc., Delaware, USA). Both binding events in the presence and absence of GSH are spontaneous enthalpically-driven and entropically unfavourable. In both instances, the dissociation constant; K_d is in the micromolar range, and the reaction stoichiometries correlate to one BSP molecule per protein dimer. The scheme below shows the heats of dilutions obtained from BSP into buffer titrations, the heat rates were subtracted from ligand into protein titration profiles to obtain the corrected heat rates corresponding to heat released when the Sj28GST: BSP complex forms. The heats of dilutions correspond to the heats obtained as the enzyme reaches saturation on the ligand into protein profiles (Figure 5.7)



Scheme 1: BSP into buffer titrations, raw heat rates correspond to heats of dilutions.

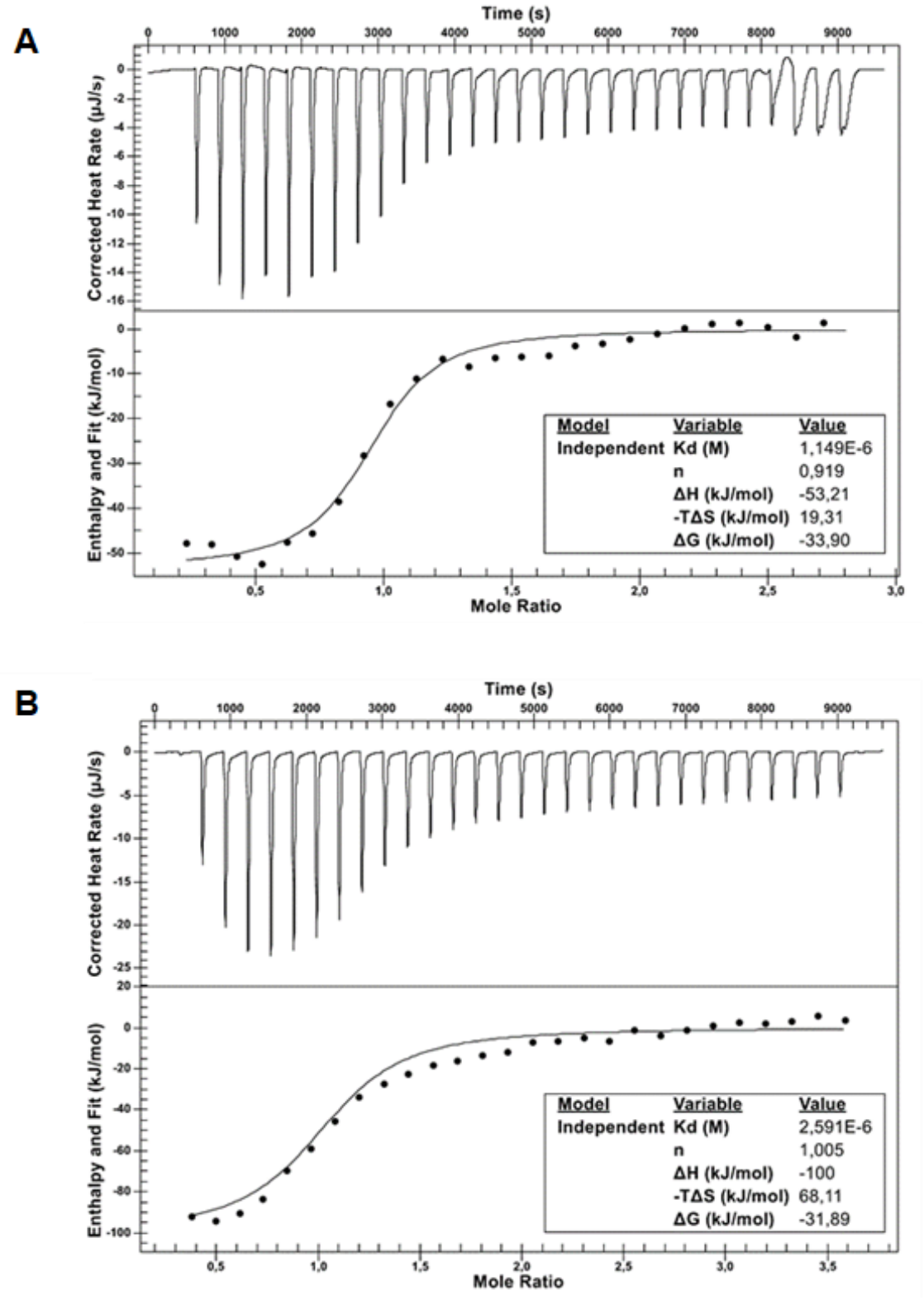


Figure 5.7 Isothermal titration profile of BSP binding to Sj28GST.1.09 mM of BSP was titrated into 58 µM of Sj28GST in incremental titrations of 5 µL each. Experiments were performed in 1×PBS buffer with 1 mM TCEP and 2 mM EDTA; pH 6.5 at 25°C. **A.** Titration experiments performed in the absence of GSH **B.** Titration experiments performed in the presence of 1mM GSH. Top panels show the area after each injection, bottom panels show binding isotherms of the integrated areas versus the molar ratio of BSP per protein monomer. The data was corrected for heats of dilutions and plotted using the NanoAnalyze software and fitted using an independent model.

5.8 Conformational stability studies: urea-induced equilibrium studies

Urea was used as a denaturant to determine the conformational stability, $\Delta G(H_2O)$ of Sj28GST. The final urea concentration required to unfold 1 µM of protein completely was 6 M incubated for 1 hour. Figure 5.8A shows that the unfolding pathway is completely reversible since the measured tryptophan fluorescence spectrum of unfolded and refolded samples is identical.As shown by Figure 5.8B, the tryptophan fluorescence spectrum of native and unfolded protein showed a shift in the maximum fluorescence intensity from 343 to 351 nm, this was coupled by a 63% increase in the quantum yield, indicating exposure of the tryptophan residue to the polar solvent as the protein unfolds. The urea denaturation curve (Figure 5.8C) was then plotted from unfolding and refolding experiments at varying urea concentrations from 0 – 8 M. Two signals were used to measure the unfolding pathway, the first was the ratio of the tryptophan fluorescence of the unfolded (351 nm) to folded (343 nm) protein, and the second was the percentage decrease in enzyme activity using the CDNB-GSH conjugation assay.

The linear extrapolation method (Figure 5.8D) was used to obtain the native dimer's stability and the C_m and *m*-value, which was 2.6 M, 4.7 kcal.mol^{-1} and 1.8 kcal.mol^{-1}M^{-1} respectively. These values could only be determined from the tryptophan fluorescence curve. There were not enough values in the transition region for the enzyme activity denaturation curve for the accurate extrapolation of $\Delta G°(H_2O)$.

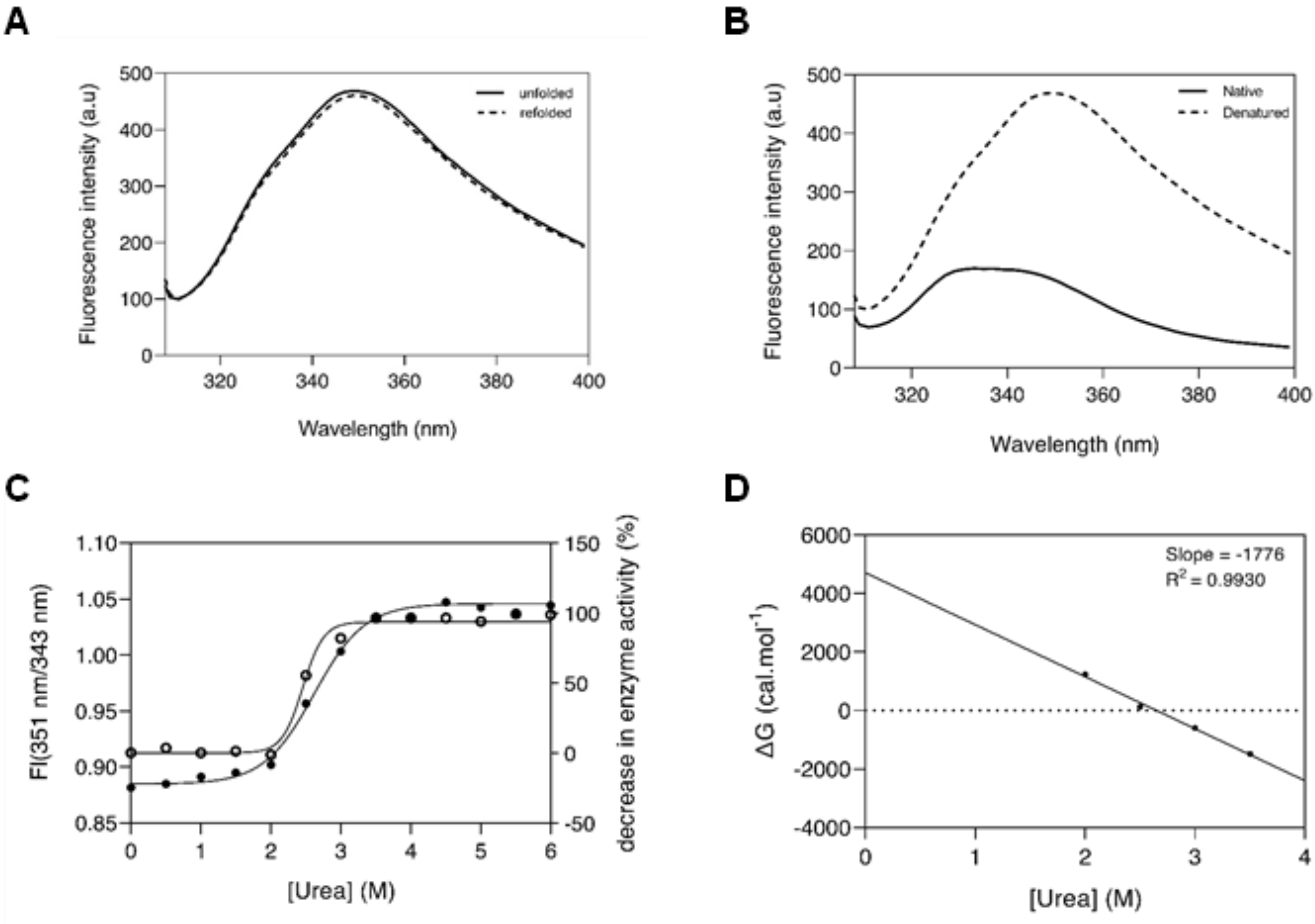


Figure 5.8 Summary of conformational stability studies for Sj28GST. **A.** The reversibility of Sj28GST unfolding measured by tryptophan fluorescence. Unfolded sample (solid line) in 0.5 M urea, refolded sample (dotted line) prepared from protein stock containing 6 M urea diluted to a final concentration 0.5 M. **B.** Intrinsic tryptophan fluorescence spectrum of a 1 µM protein solution in its native (solid line) and denatured (dashed line) state with 6 M urea. The maximum emission wavelength shifts from 343 nm to 351 nm coupled by a 63% increase in the fluorescence intensity in the presence of denaturant. **C.** The urea denaturation curve for 1 µM Sj28GST measured using the ratio of tryptophan fluorescence (solid circles) and loss off enzyme activity (open circles). The solid lines are best fits obtained from a non-linear least squares regression model. **D.** The calculated free energy change for each point in the transition region plotted against the concentration of urea. The linear equation was used calculate the conformational stability of the protein at 0 M urea.

Chapter 6
Computational results

6.1 Molecular modelling studies

Because there are no solved structures of Sj28GST available to date, a homology model of the protein was generated from the amino acid sequence. Sj28GST has the highest sequence homology (77%) to Sh28GST, and a homology model was therefore generated using the SWISS-MODEL online modelling tool (Waterhouse et al., 2018)(Figure 6.1A). The generated model was validated using PROCHECK, and the Ramachandran plot obtained indicates the absence of any phi and psi angles in unallowed regions (Figure 6.1B). Induced-fit ligand docking of ANS was performed to determine the most-stable poses of the two ligands on the Sj28GST model structure. All generated poses (15 for ANS and 17 for BSP) showed preferential binding to a site at the enzyme's dimer interface (Figure 6.2 A and B). In addition, the glide score and glide Emodel scores for all the poses were negative, indicating spontaneous binding. Lastly, the key interactions involved were polar, including three hydrogen bonds with ANS and six with BSP. A π-cation interaction between arginine 16 of chain A and a phenyl group in both ligands was also produced from the highest-scoring poses (Figure 6.2C).

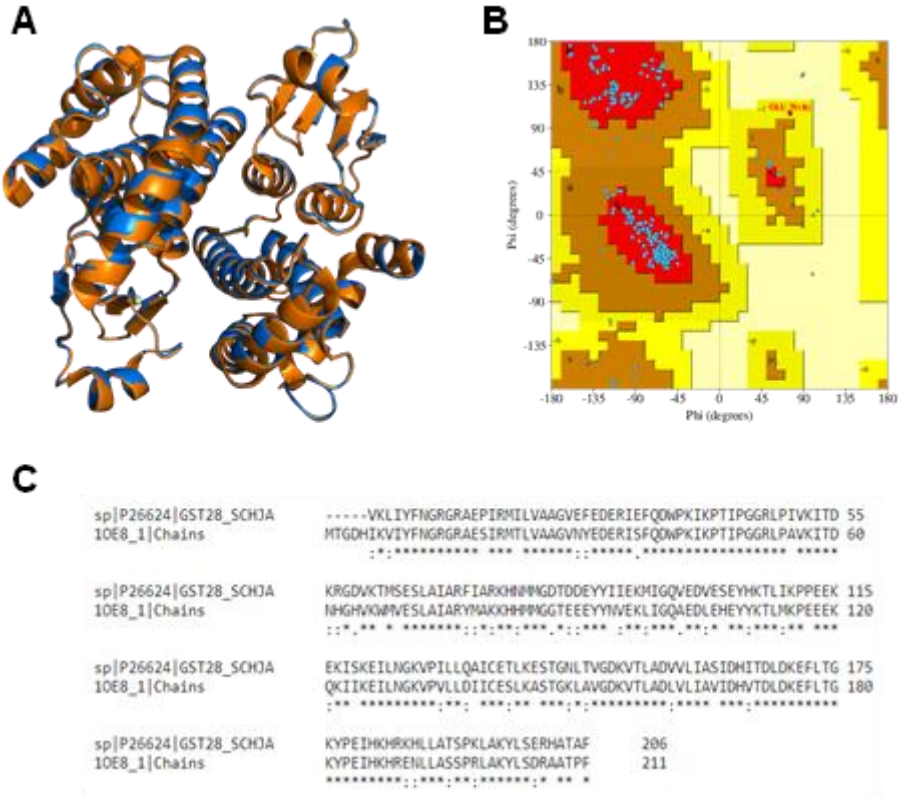


Figure 6.1 Homology modelling, validation, and sequence alignment of Sj28GST. **A.**Structure alignment of predicted homology model (Blue) and template (PBD ID: 1OE8) (Orange) generated using the SWISS-MODEL server and generated in PyMOL. **B.**Ramachandran plot of predicted Sj28GST homology model generated using Procheck on PDBsum, there are no backbone angles in disallowed regions. **C.** Sequence alignment of Sj28GST with template Sh28GST generated using Clustal Omega, the two enzymes show a sequence homology of 77%.

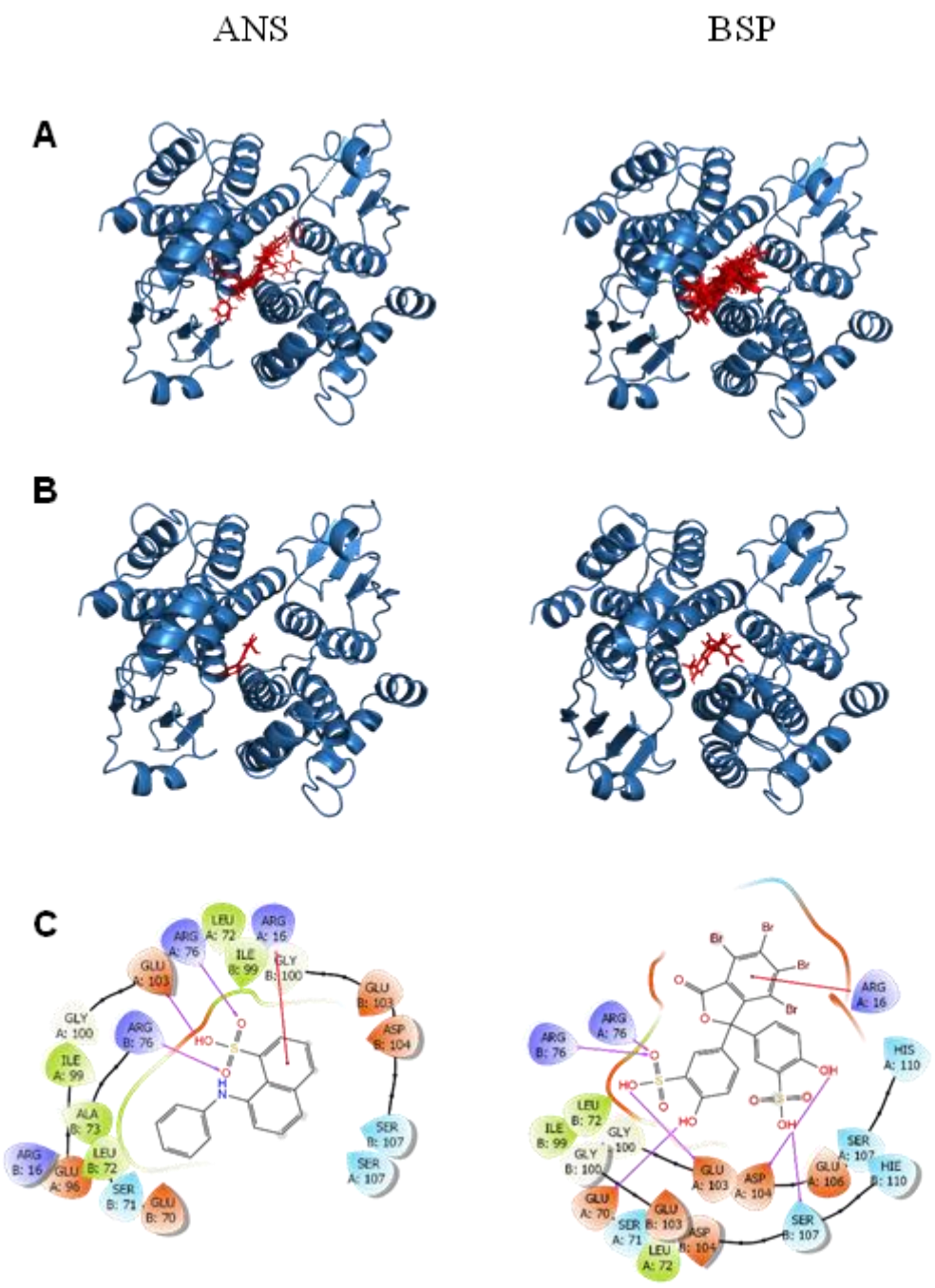


Figure 6. 2 Induced fit ligand docking of ANS and BSP to Sj28GST. **A.** Ribbon diagram showing multiple poses generated from the molecular docking, all poses show binding of both molecules (red) at the dimeric interface of Sj28GST. **B.** Ribbon diagram of the best-scoring poses of ANS and BSP to the dimeric interface of Sj28GST **C.** 2D ligand interaction plot of ANS and BSP at their binding sites. Residues in green correspond to hydrophobic side chains, red residues correspond to negatively charged side chains, light blue residues correspond to polar side chains, dark blue residues correspond to positively charged side chains. Purple lines are hydrogen bonds and red lines are pi-cation interactions. The diagram was generated in Maestro.

6.2 Molecular dynamics simulation studies

250 ns molecular dynamics simulations were conducted with the top-scoring poses from the induced fit ligand docking. Descriptive statistics of the average total and potential energies are comparable for the apo, Sj28GST:ANS and Sj28GST:BSP structures, confirming that all systems were equilibrated since the energies were well-conserved over the 250 ns simulations (Table 3). A progress plot of the root means square deviation (RMSD) for the alpha carbons is comparable across all three structures (Figure 6.3A). The RMSD remains constant after 50 ns, indicating that there is no deviation in the motion of the alpha carbons upon the binding of ANS (3.086 ±0.01) and BSP (2.896 ±0.01) with respect to the Apo (2.985 ±0.01) enzyme. This indicates that insignificant conformational changes occur on the protein dimer upon binding. Another key parameter observed from the simulation analysis was the radius of gyration (Rg). The Rg is an indication of the compactness of the structure. Assessing changes in the Rg over the simulation period gives insights into any conformational deviations resulting from a ligand-binding event. The average Rg is 21.6 Å for all three simulations (Figure 6.3B), suggesting no major spatial changes in the Sj28GST dimer occur when ANS and BSP bind. Lastly, the per-residue RMSF (root means square fluctuation) of the alpha carbons are in agreement with the analysis of the RMSD and Rg; the RMSFs are closely superimposable for the Apo and ANS/BSP complexes (Figure 6.3C), showing that there are no major fluctuations in the enzyme dimer during binding. A plot of the RMSF of the ligands with respect to the protein highlights key residues involved (Figure 6.3D). The contributions of these residues are also summarised in Figure 6.4.

Table 3: Descriptive statistics for the simulation quality analysis

	Total energy			Potential energy		
	Average	Stdev	Slope (ps^{-1})	Average	Stdev	Slope (ps^{-1})
Apo	-127781	987.6	0.0130	-159584	492.9	-0.0002
ANS	-127402	1005	0.0133	-159300	458.1	-0.0002
BSP	-127525	959.1	0.0126	-159166	372	-0.0003

Stdev is the standard deviation. Averages are computed from per ps values over 250 ns.

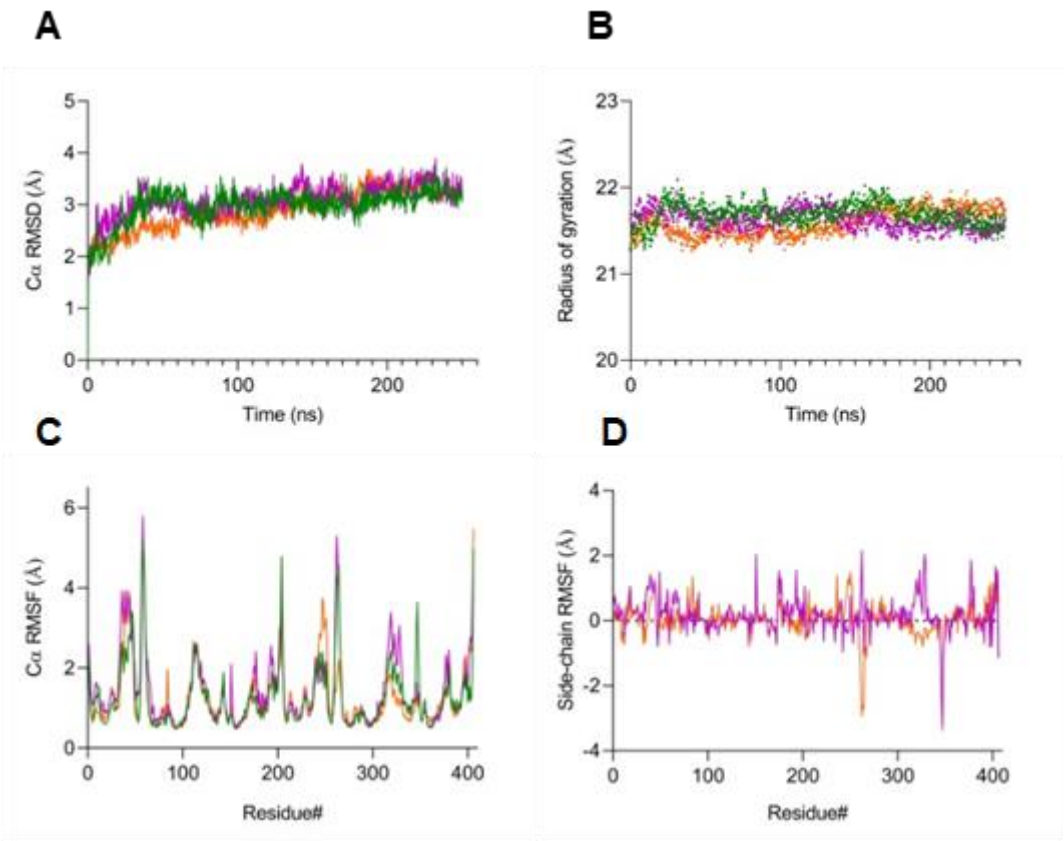


Figure 6.3 Summary of the simulation trajectories over 250 ns. The Apo structure (green), ANS-complexed strucutre (purple) and BSP-complexed structure (orange) are all plotted on the same set of axes for comparison **A.** The root means square deviation of the alpha carbons as a function of time. **B**. The radius of gyration as a function of time **C.**The root means square fluctuations of the alpha carbons as a function of time.**D**.The root means square fluctuation of the the two ligands with respect to the protein dimer as a function of time.

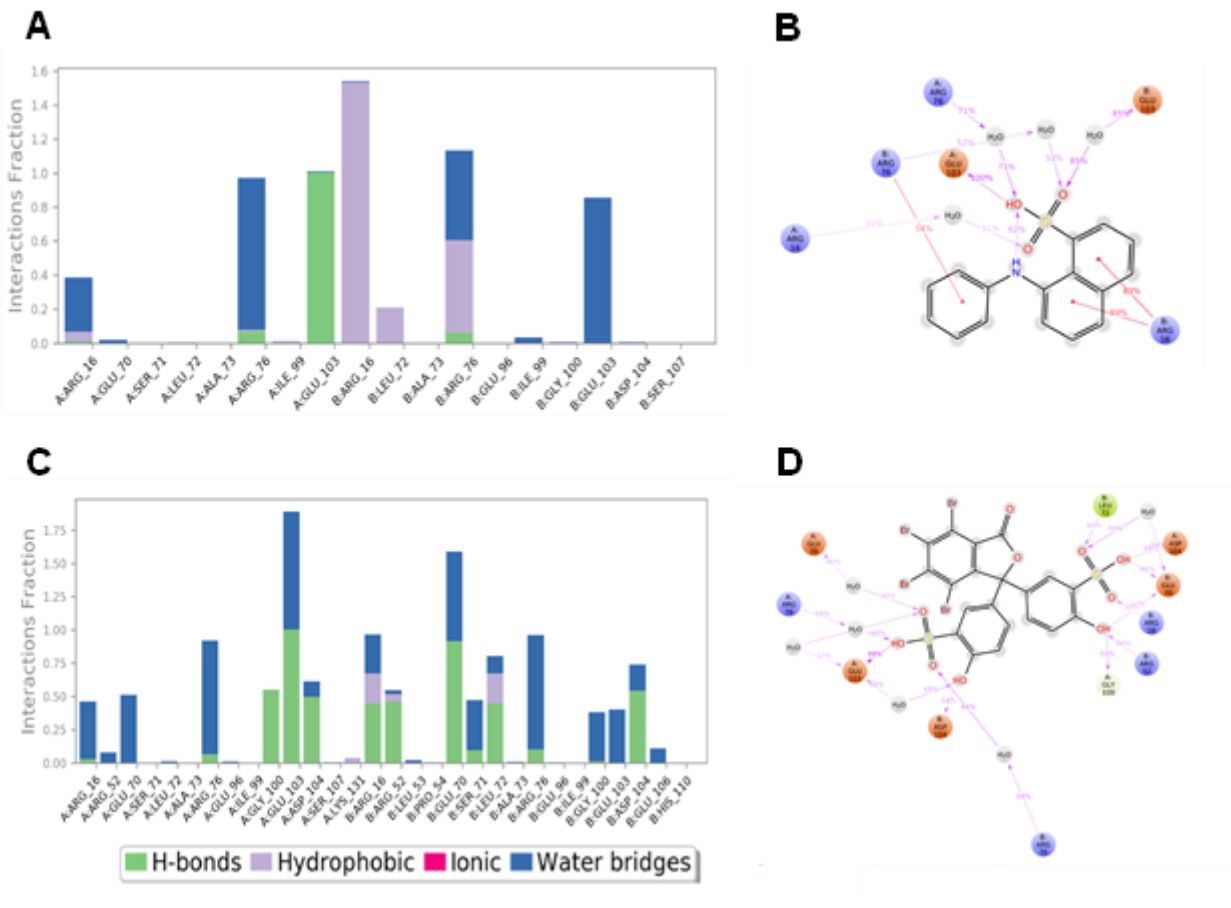


Figure 6.4 Summary of key interactions involved in ANS and BSP binding to the Sj28GST dimer interface. **A.** Interaction fractions for ANS binding. The interaction is primarily stabilised by non-polar hydrophobic interactions and water bridges. **B.** 2D ligand interaction plot of ANS bound to Sj28GST. **C.** Interaction fractions for BSP binding, which is predominantly characterised by hydrogen bonds. **D.** 2D ligand interaction plot of BSP bound to Sj28GST.

Chapter 7
Discussion

The unacknowledged impact of neglected diseases such as schistosomiasis threatens the life quality and expectancy of affected populations and the economic growth of endemic regions, especially in developing African countries. This study aimed to investigate the inhibition of the 28-kDa isoform of GST from *Schistosoma japonicum* (Sj28GST) using BSP, a well characterised cytosolic GST substrate or inhibitor. This aim was achieved by the expression, purification and quantification of the enzyme followed by structural, functional, thermodynamic, conformational stability and computational studies.

7.1 Overexpression, purification and quantification of Sj28GST

The pET vector system containing the full-length DNA sequence of Sj28GST was employed to overexpress recombinant Sj28GST using competent T7-express cells. Expression conditions used were adopted from previous overexpression of Sj26GST (Pooe et al., 2021). A small-scale sample induction confirmed that the IPTG concentration and temperature used was sufficient to induce the lacUV5 promoter, which was highly fine-tuned as there was no protein in the uninduced controls (Figure 5.1A). SDS-PAGE analysis also showed that the protein is highly soluble (Figure 5.1B). The presence of faint bands in the insoluble fraction of large-scale overexpression may have resulted from insufficient washing of the pellet samples during fractionation (Figure 5.1C). Aggregation of a small concentration of protein during overexpression is unlikely as the sample induction only shows bands in the supernatant. Also, cell cultures were cold-shocked before induction with IPTG. It has been shown that dropping culture temperatures before induction prevents protein misfolding into inclusion bodies (Qing et al., 2004). During overexpression, a relatively low temperature (30°C) was also maintained to minimise aggregation.

During protein structural-functional research, it is vital to produce high yields of recombinant protein and highly pure protein samples to ensure the integrity of the results obtained from downstream analysis. Glutathione-agarose affinity chromatography was employed in this study to purify clarified supernatants and obtain highly pure Sj28GST. Because glutathione is the natural ligand of GSTs, the binding affinity between the desired protein and the column is high, allowing for highly selective binding. Bound protein was eluted from the column matrix by using a glycine-NaOH buffer at a pH of 10. Reduced glutathione may be the practical option

for elution; however, it would be strenuous to completely dialyse any excess glutathione out of protein samples, making it difficult to determine the concentration of GSH present in downstream enzyme assays.

The theoretical molecular weight of Sj28GST generated by the ProtParam online bioinformatics tool is 23.4 kDa (Gasteiger et al., 2005). ProtParam calculates the theoretical molecular weight from the amino acid sequence using the net isotopic mass of each amino acid. The calculated subunit molecular weight of purified Sj28GST from a standard curve of relative migration distances on an SDS-PAGE gel was 28.4 kDa (Figure 5.1). The theoretical and predicted molecular weight discrepancies are due to the number of amino acids used in the available sequence. Only 206 amino acids were detected for Sj28GST, deduced from corresponding cDNA clones (Henkle et al., 1990). GSTs are on average 211 amino acids long and the predicted size of 28.4 kDa, agrees with the expected subunit size of 28.5 kDa for helminth GST isoforms (Taylor et al., 1988; Walker et al., 1993).

The presence of distinct, clear bands on SDS-PAGE gels of purified samples showed that the protein was highly pure. Very faint bands are visible in lanes with highly concentrated samples, which correspond to the dimeric form of the protein (Figure 5.1). Under reducing SDS-PAGE conditions, higher-order oligomeric states should not be visible on the gel due to denaturation by SDS-PAGE and the reducing agent, β-mercaptoethanol. Therefore, these bands may be visible due to incomplete denaturation during sample preparation, especially in fractions where the protein concentration was very high. A UV spectrum of purified protein was also measured to assess absorption by the aromatic residues, phenylalanine, tyrosine, and tryptophan, as well as the presence of any aggregation or contaminants in the protein sample (Figure 5.2B). The peak at 280 nm represents absorption by tryptophan and tyrosine residues, and the shoulder at 260 nm represents absorption by phenylalanine residues, of which there are six in the Sj28GST sequence (Henkle et al., 1990). Protein samples that do not contain aggregates do not absorb light above 350 nm (Raynal et al., 2014). The UV spectrum shows that the protein is aggregate-free. The calculated A_{260}/A_{280} ratio is 0.64. Nucleic acid-free protein samples should have a ratio of around 0.57 (Glasel, 1995). The slightly high ratio obtained for the purified sample is due to the high proportion of phenylalanine residues relative to the tyrosine and tryptophan residues in the protein monomer and not necessarily as a result of nucleic acid contamination.

7.2 The secondary structure of Sj28GST is predominantly alpha-helical

Far-UV circular dichroism was used as a structural probe to ensure that purified Sj28GST was correctly folded according to its expected secondary structural content. Cytosolic GST proteins are known to be predominantly alpha-helical proteins with around four beta strands sandwiched between six to eight alpha-helices in the N-terminus and a solely alpha-helical C-terminus (Dirr et al., 1994). The Far-UV CD profile of Sj28GST showed troughs at 208 nm and 222 nm and a peak at 295 nm, all characteristic of a predominantly alpha-helical protein (Greenfield, 2006). This confirmed that the secondary structural integrity of the enzyme was not compromised during recovery from the soluble fraction. The secondary-structural implications of BSP on Sj28GST could not be studied using this technique. This is because the drug has limited solubility in water, and stock solutions were prepared using the polar solvent, DMSO. DMSO has strong absorption in the far-UV region, which would interfere with the observed Far-UV CD profile.

7.3 ANS is displaced by BSP from Sj28GST

Extrinsic ANS studies were employed to probe for the binding of BSP to available hydrophobic sites on the Sj28GST surface. ANS has been extensively used as an extrinsic probe for binding to non-polar protein surfaces. This is due to the dependence of the molecule's excited state on the polarity of the environment. The non-polar excited state is a high energy state observed from a blue shift to shorter wavelengths accompanied by an increased quantum yield relative to free, polar solvent-exposed ANS (Stryer, 1968)(Figure 3.3). It should be noted that ANS binding to GSTs does not affect the conformational stability of the protein, and thus no structural changes are introduced by the interaction (Bico et al., 1995; Sluis-Cremer et al., 1998).

Figure 5.4 illustrates that ANS binds hydrophobically to Sj28GST, with an emission maximum that shifts from 518 nm to 487 nm, coupled by an increase in the quantum yield compared to free ANS in solution. The emission maximum of ANS bound to Sj28GST is comparable to that of ANS bound to hGSTA1-1 (475 nm), indicating that the ANS binding is not completely hydrophobic, as compared to the highly hydrophobic binding of ANS to apomyoglobin (545 nm – 454 nm) (Sayed et al., 2002; Stryer, 1965). The introduction of BSP to the protein-ANS solution results in a 68% decrease in the observed quantum yield, indicating that the ANS binding is displaced from its binding site/s by the drug. It has been reported that BSP has a higher affinity for GSTs relative to ANS (Bico et al., 1995; Yassin et al., 2004).

A previous study on the human alpha and pi class GSTs has proposed that the ANS binding site is at or near the enzyme's subunit interface. This was shown by fluorescent-resonance energy transfer studies, with distance values that coincide with crystallographic values obtained from the crystal structure of Sj26GST with PZQ (Sluis-Cremer et al., 1996). Another thermodynamic study by (Kolobe et al., 2004) has shown that ANS binds to the human class alpha GST with a binding stoichiometry of two ANS molecules per dimeric protein.

In this study, the ANS fluorescent studies for Sj28GST were repeated in the presence of 1 mM GSH and GTX to observe any differences in the maximum emission wavelength in instances where the G-site and both the G- and H-site were unavailable. Besides, physiological GSH concentrations range from 1 mM-10 mM and would therefore be saturating towards the G-site. All fluorescent spectra are identical for ANS binding and displacement in the presence and absence of GSH and GTX, which suggest that ANS binds to the protein and is displaced by BSP at the same site, even when the G- and H-site are blocked. Therefore, it can be rationally proposed that a site at the enzyme's dimer interface is the main binding site of ANS binding and displacement by BSP.

7.4 BSP inhibits the CDNB-GSH conjugation activity of Sj28GST

The CDNB-GSH conjugation assay (Habig and Jakoby, 1981) was employed in this study to characterise the functional implications of BSP on the activity of Sj28GST. This study is the first to describe the steady-state kinetic parameters of the inhibited and uninhibited enzymes. A previous study has shown that the 26-kDa GST isoform from *Schistosoma japonicum* (Sj26GST) and the 28-kDa GST isoform from *Schistosoma mansoni* (Sm28GST) follow a random sequential bi-substrate catalytic mechanism (Walker et al., 1993). Substrate specificities have been used as class-distinguishing markers for mammalian GSTs. However, in the case of parasite GSTs, the substrate and inhibitor activities overlap across classes. (Walker et al., 1993) The specific activity of Sj28GST in the presence of BSP decreased almost entirely from 60.4 ± 1.82 µmol min^{-1} mg^{-1} to 0.0742 ± 0.03 µmol min^{-1} mg^{-1} (Table 2), indicating that BSP is an inhibitor rather than a substrate of Sj28GST.

To characterise the inhibition potency of BSP on the activity of Sj28GST, the half-maximal inhibitory concentration (IC_{50}) was determined. The type of inhibition involved in inhibitor-enzyme interactions influences the IC_{50} value. Therefore, without information on the nature of inhibition, IC_{50} values are deceptive. The relationship between the IC_{50} and % inhibition depends on the mode of inhibition. Only in non-competitive inhibition is the IC_{50} independent

of the substrate concentration (Ramsay and Tipton, 2017). Steady-state kinetic assays in the presence and absence of BSP were therefore performed to determine the steady-state kinetic parameters, K_M, V_{max} and K_M/k_{cat} and the influence of BSP on these parameters (Figure 5.6). The introduction of non-linear regression in enzyme kinetics has allowed for robust and precise determination of the kinetic parameters, K_M and $V_{max,}$ directly from the Michaelis-Menten hyperbolic plots, without the need for linear reciprocal plots, which are unreliable and inaccurate (Wilkinson, 1961). Regardless, reciprocal plots such as the Lineweaver-Burke plots serve as practical tools to visualise modes of inhibition.

GST subunits consist of two main substrate binding sites, the glutathione binding site (G-site) and the electrophilic substrate binding site (H-site). When the GSH concentration is varied, the observed mode of inhibition of BSP is uncompetitive as both the K_m and V_{max} decreased in the presence of the inhibitor. This indicates that BSP only binds to the enzyme-substrate complex formed when GSH is bound to the enzyme. This observation is expected as cellular GSH concentrations are always saturating (1 mM-10 mM). Also, the enzyme's catalytic efficiency is reduced by 2.5-fold, as the formation of the enzyme-substrate complex is decreased by the binding of the inhibitor. The IC_{50} obtained was in the micromolar range (0.75 ± 0.09 µM) (Figure 5.5B), indicating a high affinity of BSP for Sj28GST compared to Sj26GST (2.38 µM) (Pooe et al., 2021). The IC_{50} value is, however, dependant on the substrate concentration used in uncompetitive inhibition (Ramsay and Tipton, 2017). It should be noted that the assay conditions used in this study were identical to those utilised for Sj26GST.

When the concentration of the electrophilic substrate, CDNB, was altered in the presence of BSP, the curves did not reach saturation at CDNB concentrations assayed. Therefore, the kinetic implications of the inhibitor on Sj28GST could not be accurately determined.

7.5 BSP binding to Sj28GST is enthalpically-driven

The thermodynamic implications of BSP binding to Sj28GST in the presence and absence of GSH suggested that the binding is enthalpically-driven. Both binding isotherms are characteristic of exothermic reactions, which fit an independent binding model per protein dimer (Figure 5.7). Also, the ΔG of the Sj28GST: BSP interaction obtained (-33 kJ mol^{-1}) agrees with that previously obtained for the Sj26GST-BSP interaction of - 30 kJ mol^{-1} (Yassin et al., 2004), suggesting that the free energy of BSP binding remains invariant and spontaneous across the schistosome GST isoforms.

Both binding events result in an unfavourable entropy (Figure 5.7). This unfavourable entropy is compensated for by a large negative enthalpy of binding, attributed to polar interactions that arise during the binding event. The unfavourable entropy must arise due to a decrease in the dynamics and degrees of freedom available during BSP binding when, resulting in a decreased conformational entropy. A study on GSH binding to Sj26GST has shown that the binding entropy is temperature-dependent and decreases to unfavorability at temperatures above 25°C, resulting in a decreased enthalpy to compensate for the unfavourable entropic loss (Ortiz-Salmeron et al., 2001).

When performing ligand into protein titrations, protonation or deprotonation of the buffer solvent may occur during the formation of the complex, which would contribute to the observed enthalpy. A phosphate buffer was used in this study as it is known to have a low enthalpy of ionization (±1 kcal mol^{-1}); therefore the experimentally obtained enthalpy would be mainly attributed to the protein-ligand interaction (Doyle et al., 1995; Ortiz-Salmeron et al., 2001). A crystal structure of Sj26GST in complex with ellagic acid has shown binding of the ligand to the enzyme's dimer interface, stabilised mainly through hydrogen bonding and van der Waals forces (Akumadu et al., 2020). A combination of empirical and computational studies has also shown that preferential BSP binding to the dimer interface of Sj26GST involves the formation of hydrogen bonds, polar contacts, salt and water bridges, and hydrophobic contacts (Pooe et al., 2021). BSP consists of two hydrogen bond donors, ten hydrogen bond acceptors and two rotatable bonds (Figure 2.9). Polar interactions between Sj28GST and the inhibitor are therefore expected to be strong contributors to the stability of the complex.

The binding stoichiometry of a titration experiment is only precisely determined when the Wiseman constant (*c*-value), the product of the association constant and the protein concentration is between 1 to 1000 (Wiseman et al., 1989).The binding of BSP to Sj28GST was moderately tight in this study (1.15 and 2.59 µM) and both *c* - values fall within this theoretical window (23 and 6.43). The obtained reaction stoichiometry of one BSP molecule per protein dimer in the presence and absence of GSH suggest the inhibitor does not bind at the G-site. BSP binds to Sj28GST at one binding site; this site is distinct from the G-site. Analysis of MD studies in the next section suggest that a site at the enzyme's dimer interface is the preferential binding site for BSP.

7.6 Computational analysis of Sj28GST: BSP binding

Induced-fit ligand docking of BSP onto the apo-Sj28GST model reveals some key insights into the ligand-binding behaviour. Firstly, the hydrophobic cleft at the enzyme's dimer interface is the preferential binding site for BSP, with all poses of the drug, including the highest-scoring pose binding to this site (Figure 6.2A).ANS docking also occurred at the dimeric interface, confirming that the displacement of ANS by BSP occurs at the enzymes dimeric interface (Section 7.3). In addition, ITC studies indicate that BSP is accommodated by one binding site on the Sj28GST dimer (Section 7.5). Due to the large-bulky nature of BSP, steric clashes will not allow binding of two stereochemically-symmetrical BSP molecules in the dimer interface. This has also been shown with a crystal structure of Sj26GST in complex with the leading anthelmintic, PZQ (McTigue et al., 1995a). The size of BSP molecule would also not allow the H-site to readily accommodate the inhibitor. Molecular docking studies therefore support empirically drawn deductions that one BSP molecule binds to Sj28GST at a site on the enzyme's dimer interface. Inhibition of the enzyme's activity is therefore due to allosteric binding of BSP.

Table 3 indicates that the average total and potential energies computed from molecular simulations of all three structures (Apo Sj28GST, Sj28GST: BSP and Sj28GST:ANS complexes) were comparable, well-conserved and energetically favourable. The three systems were therefore well-equilibrated since there were no major fluctuations in the average total and potential energies over the 250 ns simulations. The simulation quality analysis algorithm was also employed to obtain key parameters to describe the quality of the simulated systems. Firstly, the RMSD of the alpha carbons are comparable for all three systems, showing that the systems were well-equilibrated and that there were no significant changes in the level of displacement of the alpha carbons (Figure 6.3A). The Radius of gyration of the alpha carbons for all three simulations is also comparable (Figure 6.3B). With an average of 21.6 Å between the three systems, it can be concluded that the overall compactness of the Sj28GST structure is not affected upon binding of the two ligands. The RMSF of the alpha carbons is also in agreement with these observations as all RMSF's are comparable (Figure 6.3C). Overall, the simulated structures were suitable for downstream analysis as these key parameters for the ANS and BSP-complexed structures were comparable to those of the Apo- enzyme.

7.7 Sj28GST has a lower conformational stability than Sj26GST

According to previous studies, sigma and theta class GSTs have lower conformational stability relative to the alpha/mu/pi/Sj26GST type GSTs. This is a result of the stabilising effect the interdimeric hydrophobic interaction has on the overall structure of the latter (Erhardt and Dirr, 1995; Kaplan et al., 1997; Stevens et al., 1998). This study aimed to elucidate the conformational stability ($\Delta G(H_2O)$) of Sj28GST and contrast it to Sj26GST, of which its unfolding parameters and the influence of BSP on these parameters have been characterised (Yassin et al., 2004). Urea was used in this study as a denaturant. Urea mainly denatures proteins directly by breaking protein-protein interactions by forming polar contacts such as hydrogen bonds with the peptide backbone (Das and Mukhopadhyay, 2009).

To study the equilibrium unfolding pathway of a protein, it is essential to show the reversibility of the unfolding path. The unfolding of Sj28GST by urea is reversible and fit's well to a two-state model fit (Figure 5.8C)(Pace, 1986). Tryptophan fluorescence was supplemented with activity assays to confirm that the protein refolds to a catalytically active dimer. The two tryptophan residues of the Sj28GST dimer are located on a helix near the G-site. Therefore, this feature was chosen as a conformational probe for any structural changes in the active site as the protein unfolds. The maximum fluorescence intensity of the native dimer shifted from 343 to 351 nm in the presence of a denaturant. This redshift indicates that the indole ring becomes more exposed to the aqueous solvent. The shift is coupled with a 63% increase in the quantum yield. Neighbouring residues include phenylalanine 38 and lysine 45, which would quench the tryptophan excited state in the native state. The tryptophan fluorescence was completely recovered upon dilution of urea out of the denatured protein (Figure 4.8A).

The values of the ΔG (H_2O) and *m*-value obtained for Sj28GST are 4.7 kcal mol^{-1} and 1.8 kcal mol^{-1} $M^{-1,}$ respectively. These values are noteworthily low relative to those obtained for GST isoforms from the alpha, pi and Sj26GST class which range from 18 to 27 kcal mol^{-1} (Erhardt and Dirr, 1995; Kaplan et al., 1997; Wallace et al., 1998; Yassin et al., 2004). It has been shown that the *m*-value correlates well to the change in the solvent-accessible surface area once the protein unfolds (Myers et al., 1995). For a protein with an average of 404 amino acid residues, the calculated *m*-value is 4.43 kcal mol^{-1} M^{-1} and comparable values have been calculated for the alpha, pi and Sj26GST classes (Erhardt and Dirr, 1995; Kaplan et al., 1997; Wallace et al., 1998). Therefore, the *m*-value obtained in this study does not agree with the expected value. It has been shown that deviations from the two-state model result in a lowered *m*-value (Pace,

1986). The unfolding pathway was followed using two probes in this study. Both curves fit well to a cooperative two-state model. Therefore, the presence of folding intermediates is unlikely. Electrostatics is a likely cause of the low change in solvent accessible surface area of Sj28GST. A described by (Pace et al., 1990) and (Myers et al., 1995), positively or negatively charged proteins would assume more extended denatured conformations relative to neutral proteins. At a pH of 6.5, the charge of Sj28GST is more neutral relative to other GST classes with *m* - values determined at the same pH.

The equilibrium unfolding data from this study strongly suggest that the native dimer of Sj28GST is less stable than Sj26GST. This observation can be attributed to differences in the dimer interface. As shown by (Stevens et al., 1998), a class sigma glutathione transferase from the squid digestive gland unfolds via the formation of stable monomeric and dimeric intermediates with a lower ΔG (H_2O) relative to GST classes containing the lock-and-key intersubunit interaction. The exact role this interaction plays on the stability of GSTs remains unclear. However, it is reasonable to suggest that the evolution of the dimer interface comes with implications on molecular recognition and stability.

7.8 Overall conclusion, limitations and future work

This study is the first to characterise the kinetic, structural and thermodynamic implications of BSP on Sj28GST. Enzyme kinetic studies showed that BSP is a potent inhibitor of Sj28GST, showing uncompetitive binding towards the G-site. The mode of inhibition towards the H-site was not determined as the electrophilic substrate used in activity assays did not reach saturating concentrations. The secondary-structural content of Sj28GST was shown to be predominantly alpha-helical. However, future work will focus on determining the implications of BSP on the secondary structure of the protein. In the absence of a crystal structure, the location of the inhibitor-binding site can only be speculated. Extrinsic fluorescence studies, ITC and MD studies suggest that BSP binds to Sj28GST at a site distinct from the G-site, with one binding site per protein dimer. X-ray crystallography studies will be employed in future work to empirically confirm the BSP binding site, which is proposed to be at the enzyme's dimer interface in this study. Lastly, urea-induced equilibrium studies have shown that Sj28GST is less stable than Sj26GST, likely owing to differences in the enzymes' dimer interfaces. However, these studies serve as preliminary findings since the stability parameters' pH salt and temperature dependence were not investigated. The influence of BSP on the stability of the enzyme will also be investigated in future work.

References

Akumadu, B.O., Pandian, R., Olfsen, J., Worth, R., Thulo, M., Mentor, T., Fanucchi, S., Sayed, Y., Dirr, H.W., Achilonu, I., 2020. Molecular basis of inhibition of Schistosoma japonicum glutathione transferase by ellagic acid: Insights into biophysical and structural studies. Molecular and Biochemical Parasitology 240, 111319.

Anfinsen, C.B., 1973. Principles that Govern the Folding of Protein Chains. Science 181, 223-230.

Angelucci, F., Baiocco, P., Brunori, M., Gourlay, L., Morea, V., Bellelli, A., 2005. Insights into the Catalytic Mechanism of Glutathione S-Transferase: The Lesson from Schistosoma haematobium. Structure 13, 1241-1246.

Bico, P., Erhardt, J., Kaplan, W., Dirr, H., 1995. Porcine class π glutathione S-transferase: anionic ligand binding and conformational analysis. Biochimica et Biophysica Acta (BBA) - Protein Structure and Molecular Enzymology 1247, 225-230.

Bocedi, A., Noce, A., Marrone, G., Noce, G., Cattani, G., Gambardella, G., Di Lauro, M., Di Daniele, N., Ricci, G., 2019. Glutathione Transferase P1-1 an Enzyme Useful in Biomedicine and as Biomarker in Clinical Practice and in Environmental Pollution. Nutrients 11, 1741.

Bronowska, A.K., 2011. Thermodynamics of ligand-protein interactions: implications for molecular design, Thermodynamics-Interaction Studies-Solids, Liquids and Gases. IntechOpen.

Cadenas, E., Davies, K.J., 2000. Mitochondrial free radical generation, oxidative stress, and aging. Free Radic Biol Med 29, 222-230.

Cardoso, R.M.F., Daniels, D.S., Bruns, C.M., Tainer, J.A., 2003. Characterization of the electrophile binding site and substrate binding mode of the 26-kDa glutathione S-transferase from Schistosoma japonicum. Proteins: Structure, Function, and Bioinformatics 51, 137-146.

Chiumiento, L., Bruschi, F., 2009. Enzymatic antioxidant systems in helminth parasites. Parasitology Research 105, 593.

Cioli, D., Pica-Mattoccia, L., 2003. Praziquantel. Parasitology Research 90, S3-S9.

Codreanu, S.G., Thompson, L.C., Hachey, D.L., Dirr, H.W., Armstrong, R.N., 2005. Influence of the Dimer Interface on Glutathione Transferase Structure and Dynamics Revealed by Amide H/D Exchange Mass Spectrometry. Biochemistry 44, 10605-10612.

Colley, D.G., Bustinduy, A.L., Secor, W.E., King, C.H., 2014. Human schistosomiasis. The Lancet 383, 2253-2264.

Commission on Health Research for Development, 1990. Health Research: Essential link to equity in development

Cvilink, V., Lamka, J., Skálová, L., 2009. Xenobiotic metabolizing enzymes and metabolism of anthelminthics in helminths. Drug Metabolism Reviews 41, 8-26.

Das, A., Mukhopadhyay, C., 2009. Urea-Mediated Protein Denaturation: A Consensus View. The Journal of Physical Chemistry B 113, 12816-12824.

Dirr, H., Reinemer, P., Huber, R., 1994. X-ray crystal structures of cytosolic glutathione S-transferases. Implications for protein architecture, substrate recognition and catalytic function. Eur J Biochem 220, 645-661.

Dobson, C.M., 2003. Protein folding and misfolding. Nature 426, 884-890.

Dobson, C.M., Šali, A., Karplus, M., 1998. Protein Folding: A Perspective from Theory and Experiment. Angewandte Chemie International Edition 37, 868-893.

Doyle, M.L., Louie, G., Dal Monte, P.R., Sokoloski, T.D., 1995. [8] Tight binding affinities determined from thermodynamic linkage to protons by titration calorimetry, Methods in Enzymology. Academic Press, pp. 183-194.

Du, X., Li, Y., Xia, Y.-L., Ai, S.-M., Liang, J., Sang, P., Ji, X.-L., Liu, S.-Q., 2016. Insights into Protein-Ligand Interactions: Mechanisms, Models, and Methods. International journal of molecular sciences 17, 144.

Erhardt, J., Dirr, H., 1995. Native dimer stabilizes the subunit tertiary structure of porcine class pi glutathione S-transferase. Eur J Biochem 230, 614-620.

Fasman, G.D., 2013. Circular dichroism and the conformational analysis of biomolecules. Springer Science & Business Media.

Feldmeier, H., Krantz, I., Poggensee, G., 1994. Female Genital Schistosomiasis as a Risk-Factor for the Transmission of HIV. International Journal of STD & AIDS 5, 368-372.

Gabrielli, A.-F., Touré, S., Sellin, B., Sellin, E., Ky, C., Ouedraogo, H., Yaogho, M., Wilson, M.D., Thompson, H., Sanou, S., Fenwick, A., 2006. A combined school- and community-based campaign targeting all school-age children of Burkina Faso against schistosomiasis and soil-transmitted helminthiasis: Performance, financial costs and implications for sustainability. Acta Tropica 99, 234-242.

Gasteiger, E., Hoogland, C., Gattiker, A., Duvaud, S.e., Wilkins, M.R., Appel, R.D., Bairoch, A., 2005. Protein Identification and Analysis Tools on the ExPASy Server, in: Walker, J.M. (Ed.), The Proteomics Protocols Handbook. Humana Press, Totowa, NJ, pp. 571-607.

Gill, S.C., von Hippel, P.H., 1989. Calculation of protein extinction coefficients from amino acid sequence data. Analytical Biochemistry 182, 319-326.

Glasel, J.A., 1995. Validity of nucleic acid purities monitored by 260nm/280nm absorbance ratios. Biotechniques 18, 62-63.

Graham, B.B., Bandeira, A.P., Morrell, N.W., Butrous, G., Tuder, R.M., 2010. Schistosomiasis-Associated Pulmonary Hypertension: Pulmonary Vascular Disease: The Global Perspective. CHEST 137, 20S-29S.

Greenfield, N.J., 2006. Using circular dichroism spectra to estimate protein secondary structure. Nature protocols 1, 2876-2890.

Gryseels, B., Polman, K., Clerinx, J., Kestens, L., 2006. Human schistosomiasis. The Lancet 368, 1106-1118.

Gurarie, D., Wang, X., Bustinduy, A.L., King, C.H., 2011. Modeling the effect of chronic schistosomiasis on childhood development and the potential for catch-up growth with different drug treatment strategies promoted for control of endemic schistosomiasis. The American journal of tropical medicine and hygiene 84, 773-781.

Habig, W.H., Jakoby, W.B., 1981. Assays for differentiation of glutathione S-transferases. Methods Enzymol 77, 398-405.

Henkle, K.J., Davern, K.M., Wright, M.D., Ramos, A.J., Mitchell, G.F., 1990. Comparison of the cloned genes of the 26- and 28-kilodalton glutathione S-transferases of Schistosoma japonicum and Schistosoma mansoni. Molecular and Biochemical Parasitology 40, 23-34.

Huang, H.H., Rigouin, C., Williams, D.L., 2012. The redox biology of schistosome parasites and applications for drug development. Curr Pharm Des 18, 3595-3611.

Ismail, M., Botros, S., Metwally, A., William, S., Farghally, A., Tao, L.-F., Day, T.A., Bennett, J.L., 1999. Resistance to praziquantel: direct evidence from Schistosoma mansoni isolated from Egyptian villagers. The American journal of tropical medicine and hygiene 60, 932-935.

Ji, X., von Rosenvinge, E.C., Johnson, W.W., Armstrong, R.N., Gilliland, G.L., 1996. Location of a potential transport binding site in a sigma class glutathione transferase by x-ray crystallography. Proceedings of the National Academy of Sciences of the United States of America 93, 8208-8213.

Johnson, K.A., Angelucci, F., Bellelli, A., Herve, M., Fontaine, J., Tsernoglou, D., Capron, A., Trottein, F., Brunori, M., 2003. Crystal structure of the 28 kDa glutathione S-transferase from Schistosoma haematobium. Biochemistry 42, 10084-10094.

Kaplan, W., Hüsler, P., Klump, H., Erhardt, J., Sluis-Cremer, N., Dirr, H., 1997. Conformational stability of pGEX-expressed Schistosoma japonicum glutathione S-transferase: a detoxification enzyme and fusion-protein affinity tag. Protein Sci 6, 399-406.

Kolobe, D., Sayed, Y., Dirr, H.W., 2004. Characterization of bromosulphophthalein binding to human glutathione S-transferase A1-1: thermodynamics and inhibition kinetics. The Biochemical journal 382, 703-709.

Kundai, M., Myra, T., Eyrun, F.K., Panjasaram, J.N., 2018. A review of the control of schistosomiasis in South Africa. South African Journal of Science 111.

Lakowicz, J.R., 2013. Principles of fluorescence spectroscopy, 3 ed. Springer Science & Business Media.

Lapa, M., Dias, B., Jardim, C., Fernandes, C.J.C., Dourado, P.M.M., Figueiredo, M., Farias, A., Tsutsui, J., Terra-Filho, M., Humbert, M., Souza, R., 2009. Cardiopulmonary Manifestations of Hepatosplenic Schistosomiasis. Circulation 119, 1518-1523.

Leavitt, S., Freire, E., 2001. Direct measurement of protein binding energetics by isothermal titration calorimetry. Current Opinion in Structural Biology 11, 560-566.

Listowsky, I., Abramovitz, M., Homma, H., Niitsu, Y., 1988. Intracellular Binding and Transport of Hormones and Xenobiotics by Glutathiones-Transferases.

LoVerde, P.T., 1998. Do Antioxidants Play a Role in Schistosome Host–Parasite Interactions? Parasitology Today 14, 284-289.

McCord, J.M., Fridovich, I., 1969. Superoxide dismutase an enzymic function for erythrocuprein (hemocuprein). Journal of Biological chemistry 244, 6049-6055.

McCord, J.M., Keele, B.B., Fridovich, I., 1971. An enzyme-based theory of obligate anaerobiosis: the physiological function of superoxide dismutase. Proceedings of the National Academy of Sciences 68, 1024-1027.

McTigue, M.A., Williams, D.R., Tainer, J.A., 1995a. Crystal structures of a schistosomal drug and vaccine target: glutathione S-transferase from Schistosoma japonica and its complex with the leading antischistosomal drug praziquantel. J Mol Biol 246, 21-27.

McTigue, M.A., Williams, D.R., Tainer, J.A., 1995b. Crystal Structures of a Schistosomal Drug and Vaccine Target: Glutathione S-Transferase fromSchistosoma japonicaand its Complex with the Leading Antischistomal Drug Praziquantel. Journal of Molecular Biology 246, 21-27.

Mei, H., LoVerde, P.T., 1997. Schistosoma mansoni:The Developmental Regulation and Immunolocalization of Antioxidant Enzymes. Experimental Parasitology 86, 69-78.

Meyer, T., Sekljic, H., Fuchs, S., Bothe, H., Schollmeyer, D., Miculka, C., 2009. Taste, a new incentive to switch to (R)-praziquantel in schistosomiasis treatment. PLoS neglected tropical diseases 3, e357-e357.

Milhon, J.L., Thiboldeaux, R.L., Glowac, K., Tracy, J.W., 1997. Schistosoma japonicumGSHS-TransferaseSj26 Is Not the Molecular Target of Praziquantel Action. Experimental Parasitology 87, 268-274.

Myers, J.K., Pace, C.N., Scholtz, J.M., 1995. Denaturant m values and heat capacity changes: relation to changes in accessible surface areas of protein unfolding. Protein science : a publication of the Protein Society 4, 2138-2148.

Oakley, A.J., Lo Bello, M., Nuccetelli, M., Mazzetti, A.P., Parker, M.W., 1999. The ligandin (non-substrate) binding site of human pi class glutathione transferase is located in the electrophile binding site (H-site) 11Edited by R. Huber. Journal of Molecular Biology 291, 913-926.

Oliveira, P.L., Oliveira, M.F., 2002. Vampires, Pasteur and reactive oxygen species. FEBS Letters 525, 3-6.

Ortiz-Salmeron, E., Yassin, Z., Clemente-Jimenez, M.J., Las Heras-Vazquez, F.J., Rodriguez-Vico, F., Baron, C., Garcia-Fuentes, L., 2001. Thermodynamic analysis of the binding of glutathione to glutathione S-transferase over a range of temperatures. Eur J Biochem 268, 4307-4314.

Pace, C.N., 1986. Determination and analysis of urea and guanidine hydrochloride denaturation curves. Methods Enzymol 131, 266-280.

Pace, C.N., Laurents, D.V., Thomson, J.A., 1990. pH dependence of the urea and guanidine hydrochloride denaturation of ribonuclease A and ribonuclease T1. Biochemistry 29, 2564-2572.

Pace, C.N., Scholtz, J.M., 1997. Measuring the conformational stability of a protein. Protein structure: A practical approach 2, 299-321.

Pace, C.N., Vajdos, F., Fee, L., Grimsley, G., Gray, T., 1995. How to measure and predict the molar absorption coefficient of a protein. Protein Science 4, 2411-2423.

Park, S.-K., Marchant, J.S., 2020. The Journey to Discovering a Flatworm Target of Praziquantel: A Long TRP. Trends in Parasitology 36, 182-194.

Pooe, K., Worth, R., Iwuchukwu, E.A., Dirr, H.W., Achilonu, I., 2021. An empirical and theoretical description of Schistosoma japonicum glutathione transferase inhibition by bromosulfophthalein and indanyloxyacetic acid 94. Journal of Molecular Structure 1223, 128892.

Porchet, E., McNair, A., Caron, A., Kusnierz, J.P., Zemzoumi, K., Capron, A., 1994. Tissue expression of the Schistosoma mansoni 28 kDa glutathione S-transferase. Parasitology 109, 565-572.

Qing, G., Ma, L.-C., Khorchid, A., Swapna, G.V.T., Mal, T.K., Takayama, M.M., Xia, B., Phadtare, S., Ke, H., Acton, T., Montelione, G.T., Ikura, M., Inouye, M., 2004. Cold-shock induced high-yield protein production in Escherichia coli. Nature Biotechnology 22, 877-882.

Quayle, L., Appleton, C., Dickens, C., 2010. The impact of river flow regulation and manipulation on the invertebrate hosts of malaria, bilharzia and liver fluke disease. Water Research Commission: Pretoria, South Africa.

Ramsay, R., Tipton, K., 2017. Assessment of enzyme inhibition: a review with examples from the development of monoamine oxidase and cholinesterase inhibitory drugs. Molecules 22, 1192.

Raynal, B., Lenormand, P., Baron, B., Hoos, S., England, P., 2014. Quality assessment and optimization of purified protein samples: why and how? Microbial Cell Factories 13, 180.

Roberts, L.S., Janovy, J., Schmidt, G.D., 1996. Gerald D. Schmidt & Larry S. Roberts' foundations of parasitology. Wm. C. Brown, Dubuque, IA.

Rose, G.D., Fleming, P.J., Banavar, J.R., Maritan, A., 2006. A backbone-based theory of protein folding. Proceedings of the National Academy of Sciences 103, 16623-16633.

Sayed, Y., Hornby, J.A.T., Lopez, M., Dirr, H., 2002. Thermodynamics of the ligandin function of human class Alpha glutathione transferase A1-1: energetics of organic anion ligand binding. The Biochemical journal 363, 341-346.

Schwenk, M., Burr, R., Schwarz, L., Pfaff, E., 1976. Uptake of Bromosulfophthalein byIsolated Liver Cells. European Journal of Biochemistry 64, 189-197.

Seubert, J., Pohlke, R., Loebich, F., 1977. Synthesis and properties of praziquantel, a novel broad spectrum anthelmintic with excellent activity against Schistosomes and Cestodes. Experientia 33, 1036-1037.

Sluis-Cremer, N., Naidoo, N.N., Kaplan, W.H., Manoharan, T.H., Fahl, W.E., Dirr, H.W., 1996. Determination of a binding site for a non-substrate ligand in mammalian cytosolic glutathione S-transferases by means of fluorescence-resonance energy transfer. Eur J Biochem 241, 484-488.

Sluis-Cremer, N., Wallace, L., Burke, J., Stevens, J., Dirr, H., 1998. Aflatoxin B1 and sulphobromophthalein binding to the dimeric human glutathione S-transferase A1-1 : a fluorescence spectroscopic analysis. European Journal of Biochemistry 257, 434-442.

Stevens, J.M., Hornby, J.A.T., Armstrong, R.N., Dirr, H.W., 1998. Class Sigma Glutathione Transferase Unfolds via a Dimeric and a Monomeric Intermediate: Impact of Subunit Interface on Conformational Stability in the Superfamily. Biochemistry 37, 15534-15541.

Stryer, L., 1965. The interaction of a naphthalene dye with apomyoglobin and apohemoglobin: A fluorescent probe of non-polar binding sites. Journal of Molecular Biology 13, 482-495.

Stryer, L., 1968. Fluorescence Spectroscopy of Proteins. Science 162, 526-533.

Taylor, J.B., Vidal, A., Torpier, G., Meyer, D.J., Roitsch, C., Balloul, J.M., Southan, C., Sondermeyer, P., Pemble, S., Lecocq, J.P., 1988. The glutathione transferase activity and tissue distribution of a cloned Mr28K protective antigen of Schistosoma mansoni. The EMBO journal 7, 465-472.

Thomas, P.J., Qu, B.-H., Pedersen, P.L., 1995. Defective protein folding as a basis of human disease. Trends in Biochemical Sciences 20, 456-459.

Townsend, D.M., Tew, K.D., 2003. The role of glutathione-S-transferase in anti-cancer drug resistance. Oncogene 22, 7369-7375.

Trottein, F., Kieny, M.P., Verwaerde, C., Torpier, G., Pierce, R.J., Balloul, J.-M., Schmitt, D., Lecocq, J.-P., Capron, A., 1990. Molecular cloning and tissue distribution of a 26-kilodalton Schistosoma mansoni glutathione S-transferase. Molecular and Biochemical Parasitology 41, 35-44.

Valko, M., Leibfritz, D., Moncol, J., Cronin, M.T.D., Mazur, M., Telser, J., 2007. Free radicals and antioxidants in normal physiological functions and human disease. The International Journal of Biochemistry & Cell Biology 39, 44-84.

Vendruscolo, M., Zurdo, J., Macphee, C., Dobson, C., 2003. Protein Folding and Misfolding: A Paradigm of Self-Assembly and Regulation in Complex Biological Systems. Philosophical transactions. Series A, Mathematical, physical, and engineering sciences 361, 1205-1222.

Walker, J., Crowley, P., Moreman, A.D., Barrett, J., 1993. Biochemical properties of cloned glutathione S-transferases from Schistosoma mansoni and Schistosoma japonicum. Molecular and Biochemical Parasitology 61, 255-264.

Wallace, L.A., Sluis-Cremer, N., Dirr, H.W., 1998. Equilibrium and kinetic unfolding properties of dimeric human glutathione transferase A1-1. Biochemistry 37, 5320-5328.

Wang, N., Faber, E.B., Georg, G.I., 2019. Synthesis and Spectral Properties of 8-Anilinonaphthalene-1-sulfonic Acid (ANS) Derivatives Prepared by Microwave-Assisted Copper(0)-Catalyzed Ullmann Reaction. ACS Omega 4, 18472-18477.

Warren, K.S., 1982. Selective Primary Health Care: Strategies for Control of Disease in the Developing World. I. Schistosomiasis. Reviews of Infectious Diseases 4, 715-726.

Waterhouse, A., Bertoni, M., Bienert, S., Studer, G., Tauriello, G., Gumienny, R., Heer, F.T., de Beer, T.A P., Rempfer, C., Bordoli, L., Lepore, R., Schwede, T., 2018. SWISS-MODEL: homology modelling of protein structures and complexes. Nucleic Acids Research 46, W296-W303.

Wilce, M.C.J., Parker, M.W., 1994. Structure and function of glutathione S-transferases. Biochimica et Biophysica Acta (BBA) - Protein Structure and Molecular Enzymology 1205, 1-18.

Wilkinson, G.N., 1961. Statistical estimations in enzyme kinetics. The Biochemical journal 80, 324-332.

Wiseman, T., Williston, S., Brandts, J.F., Lin, L.N., 1989. Rapid measurement of binding constants and heats of binding using a new titration calorimeter. Anal Biochem 179, 131-137.

World Health Organization, 2006. Preventive chemotherapy in human helminthiasis. Coordinated use of anthelminthic drugs in control interventions: a manual for health professionals and programme managers. World Health Organization.

World Health Organization, 2015. Investing to overcome the global impact of neglected tropical diseases: third WHO report on neglected tropical diseases 2015. World Health Organization.

World Health Organization, 2016. Summary tables of mortality estimates by cause, age and sex, globally and by region, 2000–2016, in: estimates, G.s. (Ed.).

World Health Organization Geneva, 2014. Schistosomiasis: number of people receiving preventive chemotherapy in 2012. Wkly Epidemiol Rec 89, 21-28.

Yan, F., Yang, W.-k., Li, X.-y., Lin, T.-t., Lun, Y.-n., Lin, F., Lv, S.-w., Yan, G.-l., Liu, J.-q., Shen, J.-c., Mu, Y., Luo, G.-m., 2008. A trifunctional enzyme with glutathione S-transferase, glutathione peroxidase and superoxide dismutase activity. Biochimica et Biophysica Acta (BBA) - General Subjects 1780, 869-872.

Yassin, Z., Ortiz-Salmerón, E., García-Maroto, F., Barón, C., García-Fuentes, L., 2004. Implications of the ligandin binding site on the binding of non-substrate ligands to Schistosoma japonicum-glutathione transferase. Biochimica et Biophysica Acta (BBA) - Proteins and Proteomics 1698, 227-237.